2017

Normalization of Pseudo-invariant Calibration Sites for Increasing the Temporal Resolution and Long-Term Trending

Harika Vuppula
South Dakota State University

NORMALIZATION OF PSEUDO-INVARIANT CALIBRATION SITES FOR INCREASING THE TEMPORAL RESOLUTION AND LONG-TERM TRENDING

BY

HARIKA VUPPULA

A thesis submitted in partial fulfillment of the requirements for the

Master of Science

Major in Electrical Engineering

South Dakota State University

2017

NORMALIZATION OF PSEUDO-INVARIANT CALIBRATION SITES FOR INCREASING THE TEMPORAL RESOLUTION AND LONG-TERM TRENDING

This thesis is approved as a creditable and independent investigation by a candidate for the Master of Science in Electrical Engineering degree and is acceptable for meeting the thesis requirements for this degree. Acceptance of this thesis does not imply that the conclusions reached by the candidate are necessarily the conclusions of the major department.

Morakot Kaewmanee
Thesis Advisor Date

Dennis Helder, Ph.D.
Major Advisor Date

Steven Hietpas, Ph.D.
Head, Electrical Engineering and Computer Science Date

Dean, Graduate School Date

ACKNOWLEDGEMENTS

I would like to express my deepest gratitude to my major advisor, **Prof. Dr. Dennis Helder**, for introducing me to the field of radiometry, and for his vision, advice, inspiration, encouragement, and guidance throughout this project, without him this work would not have been possible. I greatly appreciate all the support he has given me during my time at South Dakota State University.

I would like to express my sincere thanks to my thesis advisor **Morakot Kaewmanee**, whose wisdom and encouragement are responsible for guiding me in the right direction. I would also like to extend my heartfelt gratitude to **Larry Leigh**, who has supported me unconditionally during my "ups and downs" throughout this project. I am grateful for his constant help, time and cooperation with this project. I am indebted to him more than he knows.

I would like to extend my special thanks to **Tim Ruggles** for his tremendous help in improving my thesis writing and providing valuable comments. I would also like to acknowledge my SDSU Image Processing Lab colleagues for providing their valuable feedback and advice.

I would like to dedicate this thesis to my father **Venkata Reddy Vuppula**, mother **Laxmi Vuppula**, brother **Satish Reddy Vuppula** and also to my "**besties**" for their support during this time.

CONTENTS

ABBREVIATIONS

AVHRR	Advanced Very High Resolution Radiometer
BRDF	Bidirectional Reflectance Distribution Function
C/A	Coastal/Aerosol
CNES	Centre National d'Etudes Spatiale
DERM	Daily Exo-atmospheric Radiance Model
DWT	Discrete Wavelet Transform
DN	Digital Number
DSL	Day Since Launch
ETM+	Enhanced Thematic Mapper+
EO-1	Earth Observing-1
ENVISAT	Environmental Satellite
GEO	Geostationary Earth Orbiting
LUT	Lookup Table
MERIS	Medium Resolution Imaging Spectrometer
MODIS	Moderate Resolution Imaging Spectroradiometer
MODTRAN	Moderate Resolution Atmospheric Transmission
NIR	Near Inferred

NOAA	National Oceanic and Atmospheric Administration
OLI	Operational Land Imager
OAM	Optimal Area Mask
ORM	Optimal Reference Map
PICS	Pseudo-Invariant Calibration Site
PNP	PICS Normalization Process
ROI	Region of Interest
STL	Seasonal Trend decomposition based on Loess
SZA	Solar Zenith Angle
SVM	Spatial Variability Map
SPTM	Spatial Temporal Mask
SWIR	Short-wave Infrared
SBAF	Spectral Band Adjustment Factor
SPOT	Satellites Pour l'Observation de la Terre
TM	Thematic Mapper
TUM	Temporal Uncertainty Map
TSM	Temporal Stability Mask
TOA	Top of Atmosphere

TSMM	Temporal Stability Mean Map
UTM	Universal Transverse Mercator coordinate system.
WRS2	Worldwide Reference System2
VNIR	Visible and Near Inferred

LIST OF FIGURES

LIST OF TABLES

ABSTRACT

NORMALIZATION OF PSEUDO-INVARIANT CALIBRATION SITES FOR INCREASING THE TEMPORAL RESOLUTION AND LONG-TERM TRENDING

HARIKA VUPPULA

2017

Given their low level of temporal, spatial, and spectral variability, Pseudo-Invariant Calibration Sites (PICS) have been increasingly desired as data sources for radiometric calibration of Earth imaging satellite sensors. The temporal resolution for PICS data acquired by any sensor is limited by the amount of time required for it to make subsequent passes over the site. Consequently, for any given PICS, it can take many years of imaging to develop a sufficient amount of cloud-free data to perform radiometric calibration; this can be especially problematic for sensors in their early years after launch. This thesis presents techniques to combine Landsat-8; normally acquiring data for every 16 days, image data from multiple PICS into a single dataset with increased temporal resolution and is called "PICS Normalization Process" or PNP. Landsat-8 Operational Land Imager (OLI) data from six Saharan desert sites were normalized to the Libya-4 reference. The normalized data were then merged into a "Super PICS" dataset, and the estimation of calibration drift was derived. The results of the Super PICS dataset show that the temporal resolution of the calibration dataset can be increased by approximately a factor of three to four times. The normalization process was performed on radiometrically and geometrically corrected image data ("L1T" product), and also on the same image data corrected for BRDF effects using a quadratic function of the solar zenith angle and TOA reflectance over a region of interest.

An additional uncertainty analysis was performed using the BRDF corrected image data based on the following parameters which are involved in this whole BRDF PICS Normalization Process: Worst-case histogram bin analysis, Temporal Uncertainty of each PICS, BRDF Super PICS uncertainty. The resulting uncertainties are within the currently accepted satellite calibration range, within 3% for all spectral bands. Overall, the process indicates a calibration drift for OLI within 0.15% per year, agreeing quite well with the calibration drift derived from the on-board calibrators.

CHAPTER 1

INTRODUCTION

1.1 Sensor Calibration

By monitoring and recording changes on the Earth's surface over a long period of time, satellite sensors have made significant contributions to the field of remote sensing [1]. Data acquired by these sensors are widely used in applications monitoring land cover change and weather. These applications require input data free of radiometric and geometric artifacts caused by changes in response of detectors in the sensor, orientation of the sensor/satellite platform with respect to the Earth's surface, atmospheric effects, etc. [1]. Radiometric and geometric calibration processes attempt to eliminate or significantly reduce the effects of these artifacts. They are, therefore, essential processes in remote sensing that should be performed as needed throughout the operational lifetime of the sensor in order to maintain data accuracy. For the purposes of this thesis, only radiometric calibration will be considered.

1.2 Radiometric Calibration

A satellite sensor measures the amount of solar energy reflected from the Earth's surface. Electronics within the sensor convert the reflected energy observed by the sensor's detectors to a series of Digital Numbers (DN) which can be displayed as an image. Radiometric calibration techniques attempt to ensure that the image DNs represent as accurate an estimate of the reflected energy as possible [1], typically at the sensor itself, which is positioned above the Earth's atmosphere (top of atmosphere-TOA). For an individual sensor, two fundamental types of radiometric calibration may be performed:

- **Relative radiometric calibration:** Differences in individual detector response are characterized and corrected. This calibration method involves determining, for each detector, the ratio of its gain to the average gain of all detectors in the detector array. Application of these ratios "equalizes" the response across all detectors in the array.
- **Absolute radiometric calibration:** Absolute gain and bias of the sensor as a whole is determined. These gains are used to convert image DNs to the corresponding values of radiance and/or reflectance measured at the Earth's surface (TOA).

  Radiometric calibration can be performed prior to launch of the satellite, when the sensor has been assembled, or at various times after satellite launch ("pre-launch" vs. "post-launch" calibration). Radiometric calibration can be performed with respect to ground measurements of surface reflectance and/or radiance ("vicarious" calibration), or with respect to data provided by sources onboard the sensor, such as lamps or solar diffuser panels ("internal" calibration). Radiometric calibration can also be performed to ensure data acquired by multiple sensors (or data from multiple sites acquired by one sensor) are accurately measuring consistent levels of surface reflectance and/or radiance ("cross" calibration).

  The radiometric calibration analysis performed for this thesis can be considered as a "relative" "cross-calibration", in that data from multiple sites acquired by a single sensor are "equalized" to a single reference level. The sites used in this analysis are known as Pseudo-Invariant Calibration Sites (PICS), which were selected for their observed low temporal and spatial variability [1].

1.3 Pseudo-Invariant Calibration Sites (PICS)

PICS have been used for monitoring the radiometric stability of satellite sensors for at least twenty years [1]. Currently, most PICS-based radiometric calibration is performed using data acquired from areas within the Sahara desert of North Africa. These sites consistently exhibit good temporal stability with respect to natural environmental or human-induced changes [2], relatively high surface reflectance, and inhibited vegetation growth due to limited rainfall.

The analysis for this thesis uses cloud-free Landsat-8 Operational Land Imager (OLI) image data acquired over six Saharan desert PICS known to exhibit temporal variability of 2% or less. The sites are identified by their World Reference System 2 (WRS2) path and row designation, as used by the Landsat series sensors. Figure 1.1 shows the location of these six PICS on the world map.

- Egypt-1 (path/row 179 / 41)
- Sudan-1 (path/row 177 / 45)
- Libya-1 (path/row 187 / 43)
- Libya-4 (path/row 181 / 40)
- Niger-1 (path/row 189 / 46)
- Niger-2 (path/row 188 / 45)

Libya-4 was selected as the reference for the analysis as it has the largest area of both temporal and spatial variability as measured in all spectral bands of OLI image data [2].

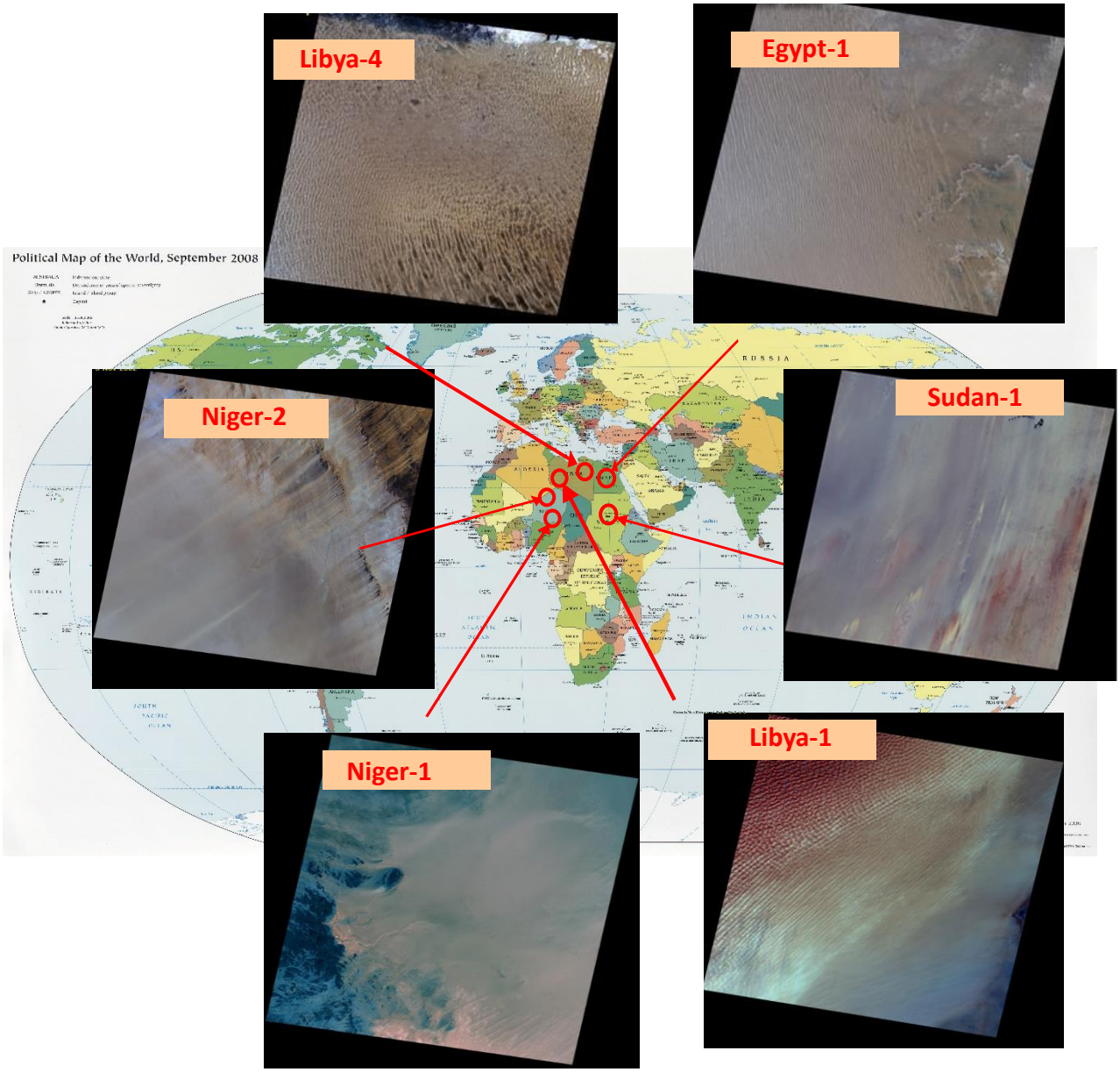

Figure 1.1. Location of 6 PICS on the world map.

1.4 Limitation of PICS and a Solution

With the Landsat-8 acquisition capability, a single PICS can be imaged once every 16 days [3]. Typically, this results in at most two useable images per month for a given site, assuming it is not obscured by clouds. More cloud-free images (Minimum of 100 for

good long-term trending) are needed for a high quality calibration. A reasonable solution to this problem is to use images acquired from multiple PICS. Figure 1.2 compares the temporal resolution, with respect to Days Since Launch (DSL), using just Libya-4 OLI image data (lower plot of blue dots) to the temporal resolution for image data acquired from all six PICS (upper plot). The gaps in the Libya-4 data, especially the gap between 600 and 800 DSL, are due to the fact that no cloud-free scenes were acquired over this site. Clearly, combining cloud-free image data from multiple sites significantly improves the temporal resolution possible for any time-series based analysis. For this selection of sites, the temporal resolution has improved by approximately a factor of three to four times.

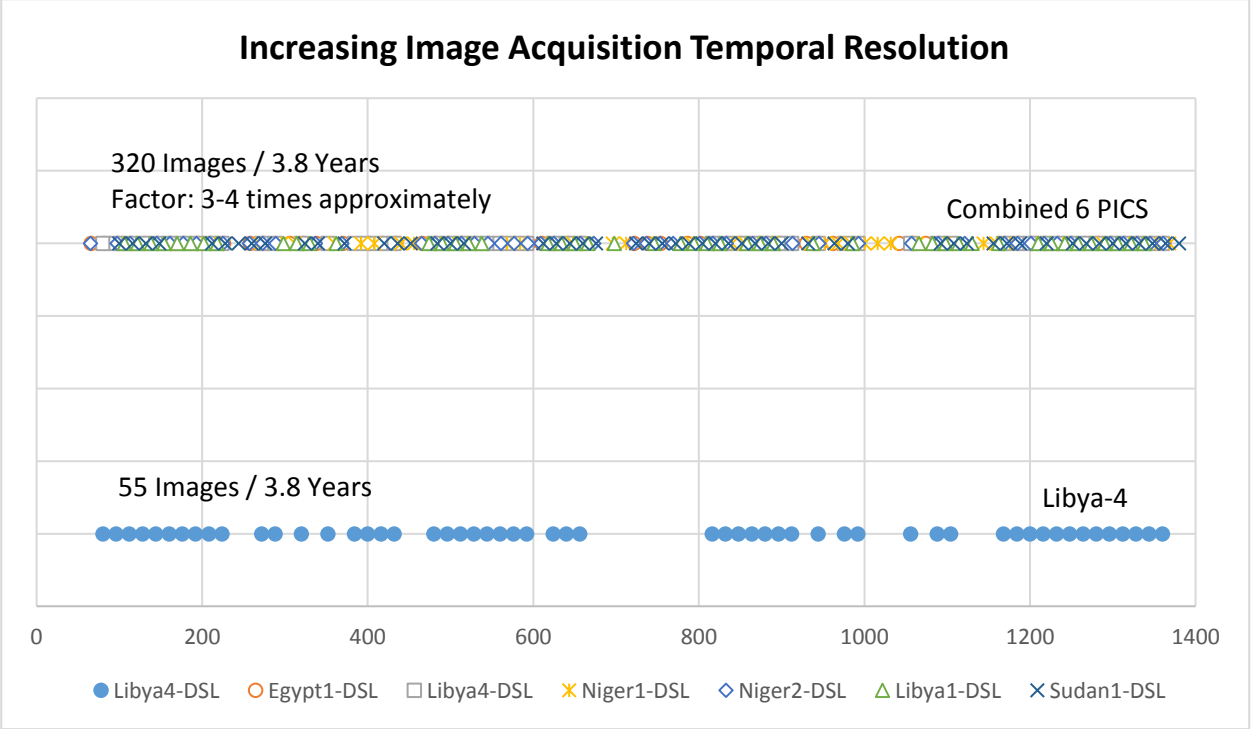

Figure 1.2. Increased temporal resolution from utilization of multiple PICS.

1.5 Thesis Objective and Summary of Results

The goal of this thesis was to develop a calibration technique that uses image data acquired from six selected PICS in order to overcome the limitation in data quantity described in Section 1.4. The technique involves normalizing all PICS data with respect to Libya-4. This normalization process is known as PICS Normalization Process or PNP, and is described in additional detail in Chapter 3. Steps to enhance the basic PNP technique, such as correction for bidirectional reflectance distribution function (BRDF) effects, drift estimation (to compare with the onboard calibrators) and uncertainty analysis are also described in Chapter 3.

Both the basic and Refined PNP techniques were applied to OLI image data to determine whether small changes in sensor responsivity could be detected in a shorter time period when multiple PICS are considered. An analysis was done to estimate the uncertainty throughout the Refined PNP technique; the analysis procedure is presented in Chapter 3. Results showing the effect of greater temporal resolution on PICS trending precision will be presented in greater detail in Chapter 4, as will results of analyses of calibration drift based on statistical tests and the overall uncertainty estimated for the Refined PNP technique. Chapter 5 summarizes the work done, conclusions, and provides recommendations for future work.

CHAPTER 2

LITERATURE REVIEW

As mentioned in Chapter 1, radiometric calibration of PICS has been performed over the past 20 years using a variety of techniques. This chapter presents a review of those techniques.

Several investigators (Thome et al. [4] and Chander [5]) have reached a consensus on the properties that a good PICS should possess. A list of these properties is presented below. Some of these have been mentioned in Section 1.4.

- High surface reflectance, in order to maximize the signal-to-noise ratio
- Temporal radiometric stability
- Flat surface spectral reflectance
- High spatial uniformity, over a sufficiently large area, in order to minimize errors due to spatial misregistration
- Lambertian surface reflectance characteristics, in order to minimize BRDF effects
- Located at high altitudes, in order to minimize atmospheric aerosol effects
- Located away from large bodies of water, in order to minimize atmospheric water vapor effects
- Located away from urban and industrial sites, in order to minimize man-made atmospheric effects (e.g. smoke, soot, etc.).

African desert sites have been the most widely used candidates for PICS-based radiometric calibration analysis. Rao and Chen [6] used a temporally radiometrically

stable Section of the Libyan Desert to monitor yearly degradation of VNIR response in the NOAA Advanced Very High Resolution Radiometer (AVHRR) sensors. An analysis of Meteosat-4 image data performed by Cosnefoy et al. [7] used twenty 100 km x 100 km North African and Saudi Arabian desert sites exhibiting 3% spatial non-uniformity. More recently, Valorge [8] used Cosnefoy's [7] sites for a temporal sensitivity analysis of SPOT sensor data; his results estimated a calibration uncertainty of less than 4%. Helder et al. [9] developed a catalog of useable worldwide PICS, with seven Saharan desert PICS (including Libya-4, Egypt-1, and Libya-1), based on a temporal stability analysis of Landsat-5 Thematic Mapper image data; results estimated overall uncertainties in these sites of less than 2% in the VNIR bands, and 2% to 3% in the SWIR bands [9]. One potential limitation of this analysis was that BRDF and atmospheric aerosol/water vapor effects at the selected sites were not accounted for. It is quite possible that these uncertainty estimates would have been lower with such corrections applied to the image data.

Hadjimitsis et al. [10] considered that atmospheric effects were a sufficiently significant limitation on calibration accuracy that they should be corrected prior to performing any calibration analysis. They used pseudo-invariant targets from Landsat-5 TM and Landsat-7 ETM+ image data to estimate atmospheric correction factors. Their ideal targets possessed the following characteristics:

- Highly homogeneous
- Smooth and horizontal, in order to be considered Lambertian

- As large in size/area as possible, in order to minimize adjacency effects and maximize ease of identification in different imagery as well as on the ground
- Distributed among low and high radiance levels

Their targets, however, included man-made materials such as concrete and asphalt. In addition, their correction factors were derived using the empirical line method, using the radiance/surface reflectance levels from two pseudo-invariant targets. Perhaps their reported accuracies would have been improved by 1) use of more than two pseudo-invariant targets; and/or 2) normalization of their target data to the radiance / reflectance level of a more precisely known target.

Mishra, Helder et al. [11] developed an absolute radiometric calibration using Terra MODIS multispectral and EO-1 Hyperion hyperspectral image data acquired over the Libya-4 PICS. Their analysis included application of a simple BRDF correction derived from the Terra MODIS image data. Their final calibration model had an estimated uncertainty on the order of 3% in all 7 bands; when applied to other sensors such as ETM+, ENVISAT Medium Resolution Imaging Spectrometer (MERIS), and OLI image data, the estimated uncertainty was on the order of 2% for all 7 bands. However, the image data used to validate this absolute calibration model did not correct for atmospheric effects.

Chander et al. [12] assessed several PICS for use as quality-assured reference standards for a PICS global network. Among the PICS under consideration as references were Libya-4 and Libya-1. Their assessment was based on analyses of cloud-free and near

simultaneous Terra MODIS and Lansdat-7 ETM+ image data pairs acquired from launch to December 2008. In addition to assessing the quality of the calibration differences between the MODIS and ETM+ sensors, they also assessed the relative stability of the sites themselves, based on derivation of linear regression models of the TOA reflectance. There were observed differences in response between MODIS and ETM+, which the authors suggest was due to a combination of differences in relative spectral response, atmospheric effects, and the overall spectral signature of the surface. An obvious seasonal variation in response could also be observed in both datasets. In addition, BRDF correction had not been accounted for in the analysis.

Morstad and Helder [13] proposed using PICS to perform long-term radiometric calibration of the Landsat-5 TM sensor. To overcome potential issues of data availability and lack of supporting vicarious calibration datasets for the Saharan desert PICS, they considered a much smaller PICS situated along the US and Mexican borders, in the Sonoran desert (WRS2 path/row 038 / 038). Thirty scenes acquired over this PICS were processed with scan-correlated-shift and memory-effect corrections, then corrected to account for relative differences in detector response. Additional corrections included date-specific sun-earth distance correction and standard sun elevation angle correction. Geometric corrections were performed in order to account for forward/reverse scan misalignment and variation in scene center coordinates. Once the scenes were sufficiently corrected, a two-step approach was used to determine the "best" region-of-interest (ROI) for each spectral band:

- Step 1: a 200 pixel x 200 pixel grid was used to identify candidate ROIs through comparison to a look-up Table (LUT) -based model.

- Step 2: a 200 pixel x 200 pixel moving window was employed near the most invariant regions identified in the grid approach in order to rank the ROIs.

The calibration models derived for the blue and green bands appeared to fit the best ROI data quite well; this did not appear to be the case for the longer wavelength bands, where the fits suggested a very small linear change. Overall, the estimated calibration uncertainties were on the order of 1% to 4%, with smaller uncertainties associated with the blue and green bands.

Kim and He [14] performed an assessment of long-term degradation in radiometric response using a time series analysis of data acquired from the Libya-4 and Sonoran PICS. In this analysis, linear regression was performed on time series data with the component due to seasonal variability removed; the Seasonal Trend decomposition based on Loess (STL) and Discrete Wavelet Transform (DWT) algorithms were used to determine the seasonal varying component. Their results showed that the STL algorithm was slightly more effective at estimating the seasonal component, with the result that overall variability in the trend data was less. No uncertainty estimates for their analysis were provided. It is quite possible that residual variability resulting from removal of the seasonal component could be reduced further using different processing techniques.

Angal, Xiong, et al. [15] developed a multi-temporal cross calibration technique for Terra MODIS and ETM+ sensors using cloud-free image pairs over the Libya-4 PICS. Their analysis developed a semi-empirical linear BRDF model and applied it to reduce effects due to viewing geometry differences. Atmospheric water vapor content was characterized using the MODIS water vapor product and corrected with a “split-window” processing

technique. In addition, differences in spectral bandpass response between the sensors were estimated from simulated TOA datasets generated by EO-1 Hyperion image data and MODTRAN simulations which used MODIS water vapor information as an input. The analyses allowed generation of spectral band adjustment factors (SBAFs). The results of their work indicated that ETM+ could be calibrated to an uncertainty on the order of 4% for bands 1 to 4 and to an uncertainty on the order of 6% and 4% for bands 5 and 7, respectively, if SBAFs were applied as part of the analysis. Without application of SBAFs, the uncertainties were on the order of 6% for bands 1 to 4 and 10% and 16%, respectively, for bands 5 and 7.

Bhatt, Doelling et al. [16] proposed that a Daily Exo-atmospheric Radiance Model (DERM) could be used to perform absolute radiometric calibration. With their method, desert PICS image data acquired by a well-calibrated "reference" Geostationary Earth Orbiting (GEO) sensor can "transfer" that calibration to a "target" GEO sensor located at the same equatorial longitude. For their analysis, Meteosats-7 and 8 were selected as the "target" GEO sensors, while Meteosat-9 was selected as the "reference" sensor. For both cases, the Libya-4 PICS was selected as their test site. A radiance-based cross-calibration of Meteosat-9 to Aqua MODIS was performed first. The DERM was developed based on this cross-calibration and applied to radiance-based cross-calibrations with Meteosat-7 and Meteosat-8. Part of the calibration analysis involved derivation of SBAFs to account for spectral response differences. A similar analysis was performed using GOES-11 as the reference sensor and GOES-10 and 15 as the targets. 1σ uncertainties for each step of the method were provided for both datasets; the largest uncertainty component was found

to come from the Aqua MODIS cross-calibration. They estimated an uncertainty on the order of 1% related to the DERM model itself. Based on the selected sensors and PICS, they estimated an overall uncertainty to their method on the order of 3%. For desert PICS at least, the approach appears to be promising.

Mishra, Helder, et al. [17] summarized the continuous calibration improvement in the solar reflective bands from the Landsat-5 TM through the Landsat-8 OLI. They documented the differences in design between the OLI and the TM and ETM+ and how those differences affect overall sensor performance, such as the significant improvement in OLI spectral bandpass and signal-to-noise ratio due to its pushbroom design and greater number of detectors. Their primary objective was to compare the accuracy of OLI vicarious calibration of PICS to the calibration provided by the on-board calibration sources, which were indicating a general drift of less than 0.1% per year across all 7 bands. Their vicarious results suggested a calibration drift of 0.7% per year for the Coastal/Aerosol band, as compared with a 0.3% yearly drift indicated by the on-board calibrators; this difference was entirely consistent with previous PICS-based calibration uncertainties. In the Blue, Green, Red, NIR, and SWIR1 bands, the vicarious drift estimates differed from the on-board calibrator estimates by approximately 0.5% per year; the SWIR2 band differences were slightly greater than 0.6% per year. In general, they estimated a lower uncertainty bound of 0.5% per year for PICS-based vicarious calibration. It should be noted, however, that atmospheric effects were not accounted for in the analysis.

From this literature it was observed that researchers have been using PICS (especially Saharan desert PICS) as calibration data sources for many years. Libya-4 in particular has been considered as a "reference" PICS, given its established temporal and spatial stability within 2% or less with respect to the bands of interest in most sensors.

The techniques proposed in this thesis will be shown to address two particular limitations in the calibration analyses summarized in this chapter:

1. The limited number of images for most sites, particularly for satellite sensors in early stage after launch, has hampered the ability to generate a consistent long-term trending record. The techniques proposed in this thesis will demonstrate that data from multiple PICS can be combined, and that this combined dataset provides sufficient temporal resolution to create a reliable long-term trending record. In addition, the proposed techniques can also provide sufficient trending information to allow vicarious calibration results comparison to various on-board calibration sources.
2. As previously reviewed, BRDF effects were not accounted for or at best corrected by models assuming BRDF to be linear in nature. As will be discussed in Chapter 3, BRDF appears to be primarily quadratic in nature. So, a quadratic BRDF will be developed to further reduce uncertainties.

The technique proposed in this thesis is expected to demonstrate uncertainty of Landsat-8 data to match or better than the satellite calibration uncertainty of approximately 3% based on the currently used desert PICS, and confirm that it is a suitable method for satellite calibration.

CHAPTER 3

METHODOLOGY

3.1 Overview of PICS Normalization Process:

As mentioned in Chapter 1, a significant limitation to using image data of a given PICS for radiometric calibration purposes is insufficient temporal resolution, as many currently operating sensors can only image the site on a weekly or bi-weekly basis. Combining image data from multiple PICS can provide increased temporal resolution, but the data must be normalized with respect to an accepted reference level in order to minimize uncertainties due to variability within and between sites. For this thesis work, an algorithm to perform this normalization has been developed. This chapter describes the proposed algorithm in greater detail. The algorithm is composed of 2 normalization steps:

- **Normalization of data for an individual PICS:** The basic idea for this step is to develop correction maps that would bring all the pixel values in a PICS image to an optimal TOA reflectance level.
- **Normalization of data across multiple PICS:** Libya-4 was chosen as the reference PICS for this step due to its previously demonstrated temporal and spatial stability. The intent of this step is to make each selected PICS "look like" Libya-4 with respect to its TOA reflectance levels.

3.1.1 Image Selection and Pre-Processing:

The input data used to develop the algorithm were cloud-free 2015 Landsat-8 OLI images acquired over six North Africa PICS (Egypt-1, Libya-1, Libya-4, Niger-1, Niger-2, and

Sudan-1); if a 2015 image for a given month was not usable, a 2013 or 2014 image from that month was used instead. The set of L1T product images was selected from the SDSU Image Processing Laboratory archive after processing through an internally developed cloud-screening algorithm [18]. All images were pre-processed to correct radiometric and geometric artifacts and converted to calibrated Digital Numbers (DN).

3.1.2 Normalization of Data for an Individual PICS:

An initial study was performed to determine the number of correction maps (maps to bring all pixels to optimal TOA level) needed for each PICS that would minimize effects due to seasonal variation within a given year and throughout multiple years. Three methods to generate correction maps were considered: i) generate one correction map by averaging an entire year's worth of image data; ii) generate an average correction map for each season (spring, summer, fall, and winter); and iii) generate a correction map for each month. Based on the variability of TOA reflectance for each method, the study found that seasonal effects were best minimized using correction maps generated for each month. Consequently, this approach for generating the required correction maps was selected for the PICS normalization process.

The following steps comprise the normalization procedure applied to a set of yearly image data for a given PICS (i.e. one image acquired during each month). The result of this within-site normalization procedure is an estimate of the optimal TOA reflectance representing the PICS, which is defined as the mean TOA reflectance within a region exhibiting 3% or better temporal, spatial, and spectral stability. The processing steps are performed for each band separately.

1. To reduce the effects of noise within the image data, apply a low-pass filter *H* (u,v) to the monthly image data *I*(i, j) as described in equation (1).

$$I'(i,j) = \sum_{\substack{0<u<165 \\ 0<v<165}} I(u+i, v+j) * H(u,v) \quad (1)$$

The filter size used in the convolution is 165x165 pixels, which corresponds to a ground area of 5x5 km. This size is selected based on a study with ROI image data indicating that the mean TOA reflectance is essentially constant over such a region. The filtered output is then effectively cropped to the same size as the original input image.

2. Arrange the monthly smoothed images in temporal order (i.e. from January to December) to form a "stack" or 3-dimensional array *I'*(i, j, t), where 'i' represents the 'line' dimension, 'j' represents the 'sample' dimension, and 't' represents the temporal dimension. For each pixel location (i, j) in *I* ', calculate the temporal mean and standard deviation according to equations (2) and (3). These will result in temporal mean and standard deviation "images" **μ** and **s**, respectively.

$$\mu(i,j) = \frac{1}{12}\left[\sum_{t=1}^{12} I'(i,j,t)\right] \quad (2)$$

$$s(i,j) = \sqrt{\frac{\sum_{t=1}^{12}(I'(i,j,t)-\mu(i,j))^2}{11}} \quad (3)$$

3. Create a Temporal Uncertainty Map (TUM) by taking the ratio **s / μ**:

$$TUM(i,j) = \frac{s(i,j)}{\mu(i,j)} \times 100 \quad (4)$$

4. Create a binary Temporal Stability Mask (TSM) by setting TUM pixels with uncertainty less than 3% to 1, and setting TUM pixels with uncertainty greater than 3% to 0.

5. Create a 3% Temporal Stability Mean Map (TSMM) by multiplying the temporal mean image **μ** created in step 2 with the binary TSM image created in step 4, as indicated in equation (5). Figure 3.1 shows an example TSMM for band 1 of the Libya-4 PICS.

$$TSMM(i,j) = TSM(i,j) \times \mu(i,j) \quad (5)$$

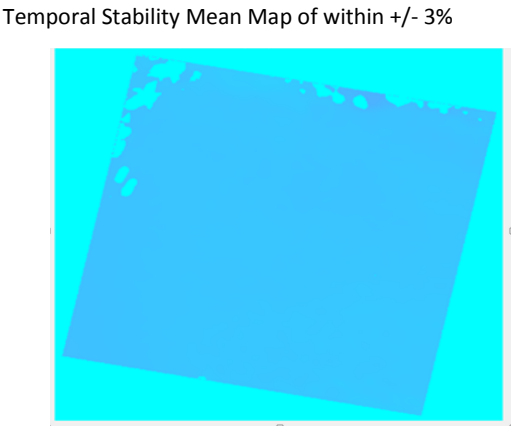

Figure 3.1. 3% TSMM for OLI C/A band of the Libya-4 PICS.

6. Generate a histogram of the TSMM created in step 5. Determine the mode TOA reflectance, ρ_{mode} (i.e. the TOA reflectance values observed most frequently) assuming a bin number of 20. Using equations (6a) and (6b) and the histogram mode, determine the range of TOA reflectance values ρ_{min} and ρ_{max} that are most frequently observed. An example histogram of the band 1 TSMM for the Libya-4 PICS is shown in Figure 3.2.

$$\rho_{min} = (1 - 0.15) \times \rho_{mode} \quad (6a)$$

$$\rho_{max} = (1 + 0.15) \times \rho_{mode} \quad (6b)$$

-0.15 to +0.15 spans 3%

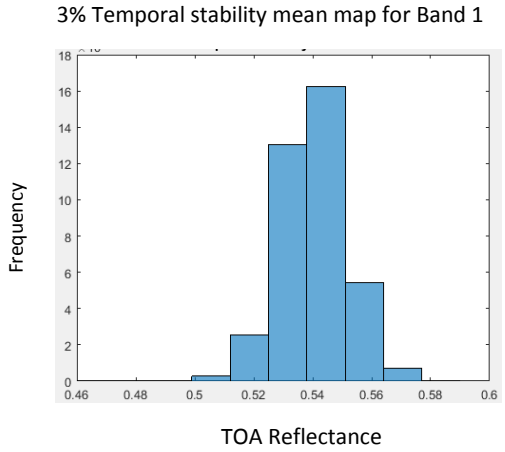

Figure 3.2. Histogram of 3% TSMM for OLI C/A band of the Libya-4 PICS.

7. In the TSMM image, create a map, TempMap, by setting the pixels with TOA reflectances outside of the range (ρ_{min}, ρ_{max}) to 0 (leaving the pixel values within the range unchanged). Then use equation (7) to calculate the temporal mean of the *N* pixels within the resulting non-zero region. The 'i' subscript in equation (7) indicates those TempMap pixels with non-zero values.

$$TemporalMean = \frac{1}{N}\sum_{i=1}^{N} TempMap_i \quad (7)$$

8. From TSMM created in step 5 and the temporal mean value calculated in step 7, create a 3% Spatial Temporal Mask (SPTM) as follows. First, create a spatial variability map, SVM, calculated as the ratio of the difference between TSMM and temporal mean to temporal mean:

$$SVM(i,j) = \frac{TSMM(i,j) - TemporalMean}{TemporalMean} \times 100 \quad (8)$$

Then, create SPTM by setting all pixels in the SVM where the value is < 3% to 1, and setting all pixels in the SVM where the value is > 3% to 0. The SPTM represents the region identified as having 3% or less spatial and temporal uncertainty. Example SPTM images generated for each band of the Libya-4 PICS are shown in Figure 3.3.

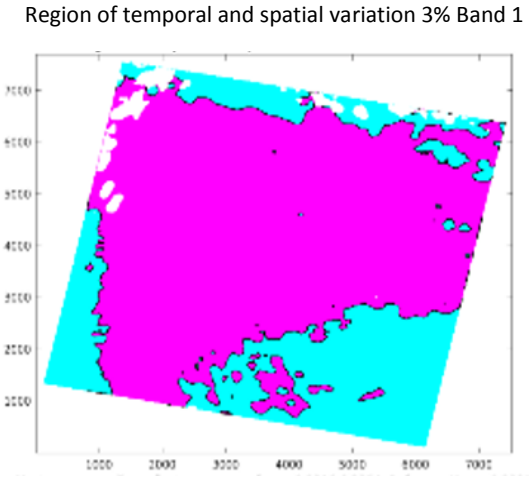

(a) SPTM, C/A Band

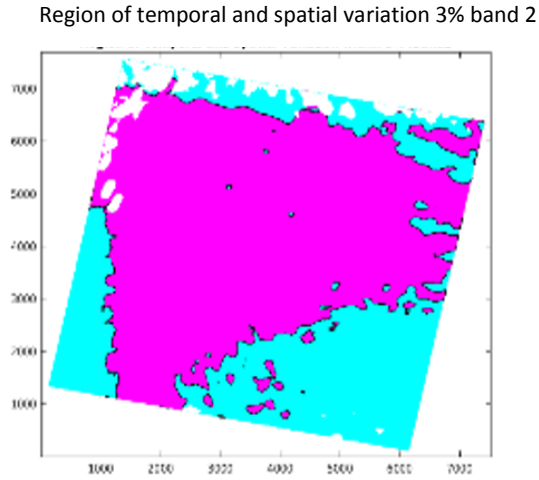

(b) SPTM, Blue Band

Where pink represents the 3% spatial and temporal stability region, blue represents 3% temporal stability region and white represents the region having more than 3% temporal uncertainty.

Region of temporal and spatial variation 3% Band 3

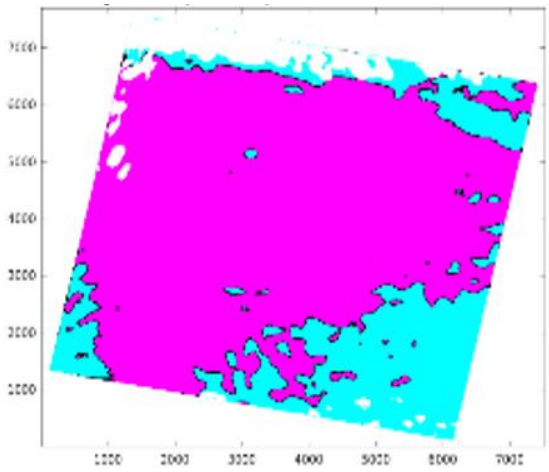

(c) SPTM, Green Band

Region of temporal and spatial variation 3% Band 4

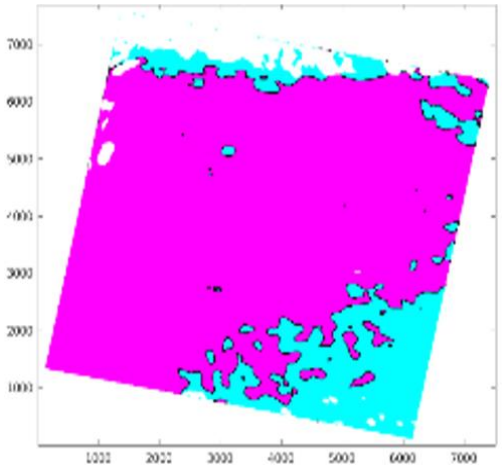

(d) SPTM, Red Band

Region of temporal and spatial variation 3% Band 5

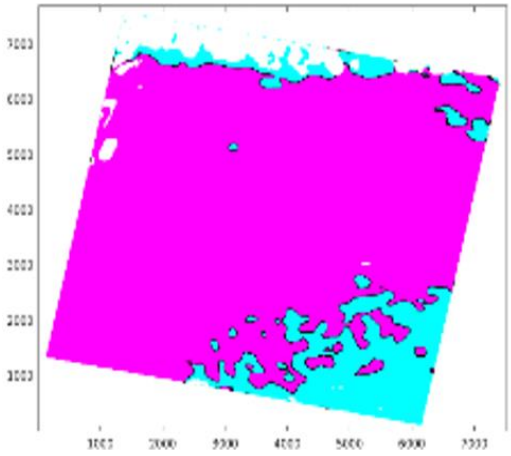

(e) SPTM, NIR Band

Region of temporal and spatial variation 3% Band 6

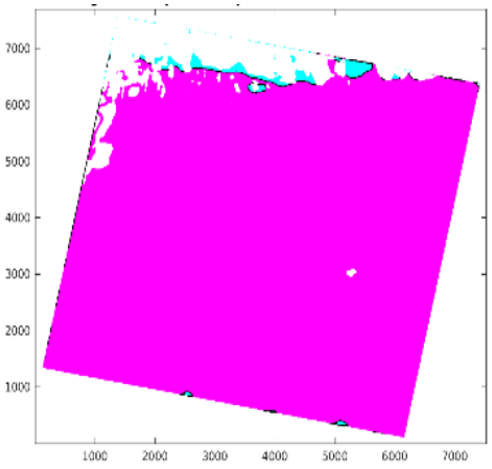

(f) SPTM, SWIR1 Band

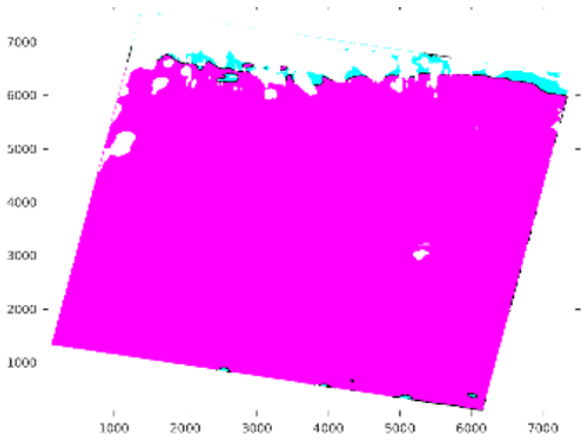

(g) SPTM, SWIR2 Band

Figure 3.3. SPTM for all OLI bands of the Libya-4 PICS.

9. At the end of steps 1-8, there should be seven SPTM images (one for each band). Using equation (9) create an Optimal Area Mask (OAM) by identifying SPTM pixels with 3% or less uncertainty that are present in all 7 bands: Figure 3.4 shows the OAM generated for the Libya-4 PICS.

$$OAM(i,j) = \begin{cases} 1, & SPTM(i,j) = 1 \; in \; all \; seven \; bands \\ 0\,, & otherwise \end{cases} \tag{9}$$

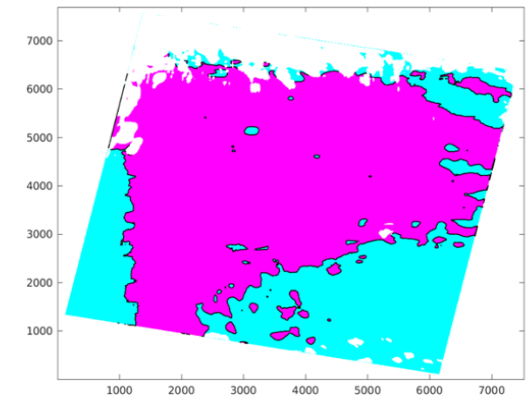

Figure 3.4 OAM for Libya-4 PICS.

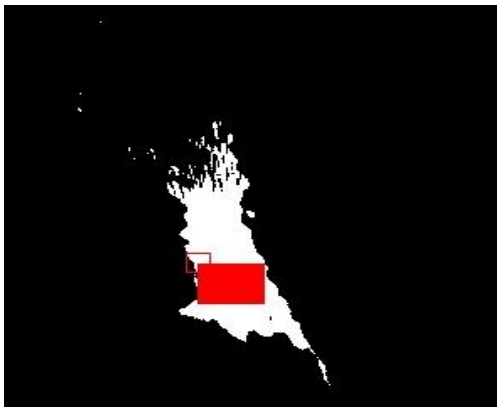

(a) ROI for Egypt-1 PICS

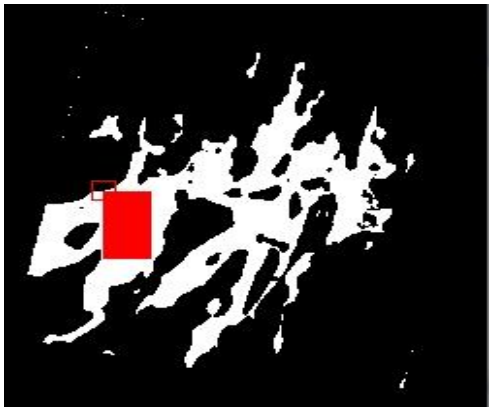

(b) ROI for Sudan-1 PICS

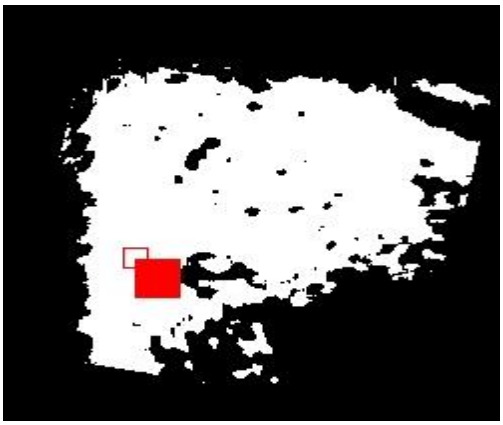

(c) ROI for Libya-4 PICS

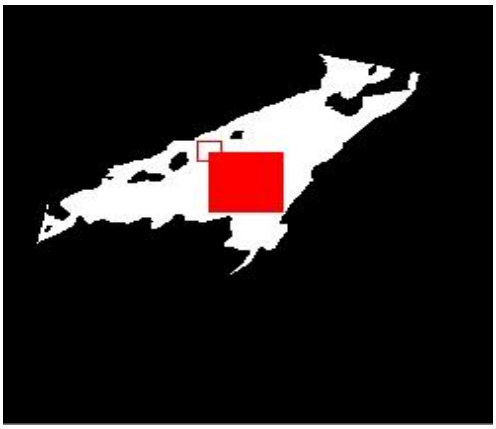

(d) ROI for Libya-1 PICS

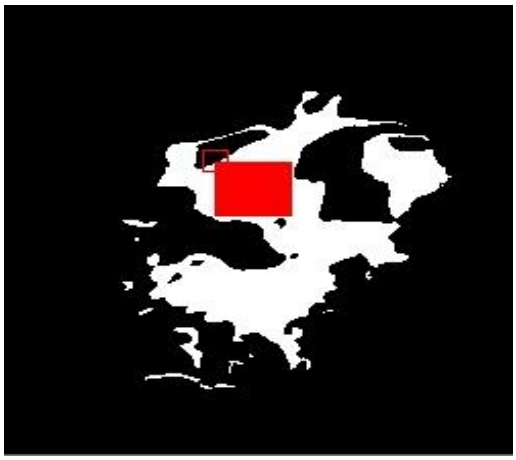

(e) ROI for Niger-1 PICS

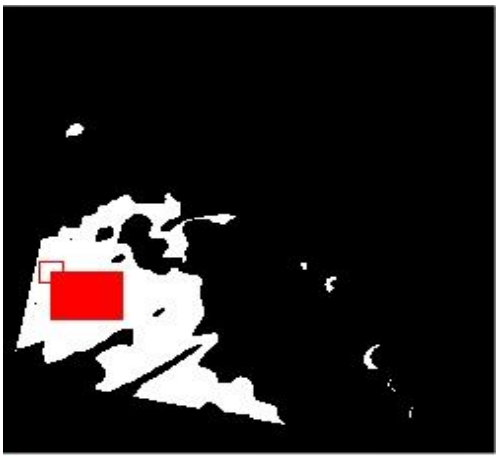

(f) ROI for Niger-2 PICS

Figure 3.5. Binary OAMs for each PICS showing in white. The solid red boxes represent the ROIs subsequently used to evaluate the PNP method's performance.

The Figure 3.5 represents the optimal region for all 6 PICS. Where white region represents the 3% temporal, spatial and spectral stability region and red boxes indicate the ROI. Coordinates for these ROI regions are tabulated in Table 3.1 in Universal Transverse Mercator coordinate system (UTM).

PICS Names	Upper Left Corner (meters)		Lower Right Corner (meters)		No. Images
Libya-4	E723825	N3171375	E743805	N3149685	62
Libya-1	E330150	N2750850	E365070	N2716860	43
Niger-1	E520470	N2271210	E555120	N2242890	46
Niger-2	E644190	N2375910	E677670	N2350590	52
Egypt-1	E431790	N3000930	E462960	N2977110	55
Sudan-1	E561570	N2405850	E584250	N2367450	62

Table 3.1. Corner coordinates defining the analysis ROIs for each PICS.

10. Multiply the OAM determined in step 9 with each band's TSMM image generated in step 5 to create each band's Optimal Reference Map (ORM):

$$ORM(i,j) = OAM(i,j) \times TSMM(i,j) \tag{10}$$

11. From the ORM images generated in step 10, calculate each band's Optimal Reference value as the mean of all non-zero pixels:

$$OptimalReference = \frac{1}{N}\sum_{k=1}^{N} ORM_k \tag{11}$$

12. Apply the Optimal Reference mean value calculated in step 11 to the smoothed image stack generated in step 2 to create the set of monthly correction map images for each band:

$$CorrectionMap(i,j,t) = \frac{Optimal\ Reference}{I'(i,j,t)} \tag{12}$$

An example correction map for month 1 in band 1 of the Libya-4 PICS is shown in Figure 3.6. All the pixel values in this correction map are very close to the optimal mean TOA reflectance value for the Coastal/Aerosol band of Libya-4. The correction map shown in Figure 3.6 is used to correct all Coastal/Aerosol band images that are acquired in January over Libya-4. Likewise, for each month, each band, and also for each PICS, the correction maps were created and used to correct Landsat-8 images since launch to 2016.

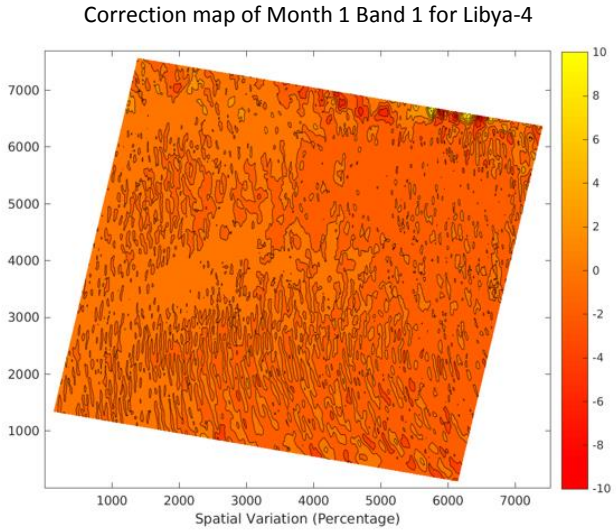

Figure 3.6. Correction map for month 1 in OLI C/A band of the Libya-4 PICS.

Figure 3.7 summarizes the steps needed to perform the within-site normalization. Image statistics (mean, standard deviation, and uncertainty) are calculated from the smoothed and temporally ordered monthly image data stack. These statistics are used to create a 3% temporal stability mean map. The histogram of the temporal stability mean map establishes the range of TOA reflectances having 3% uncertainty. A mask with pixels having 3% temporal, spatial and spectral variability is created and applied to the temporal stability mean map to determine the optimal TOA reference mean value as described in steps 6 to 11. The final correction maps are then obtained by applying the optimal TOA reference mean to each smoothed monthly image.

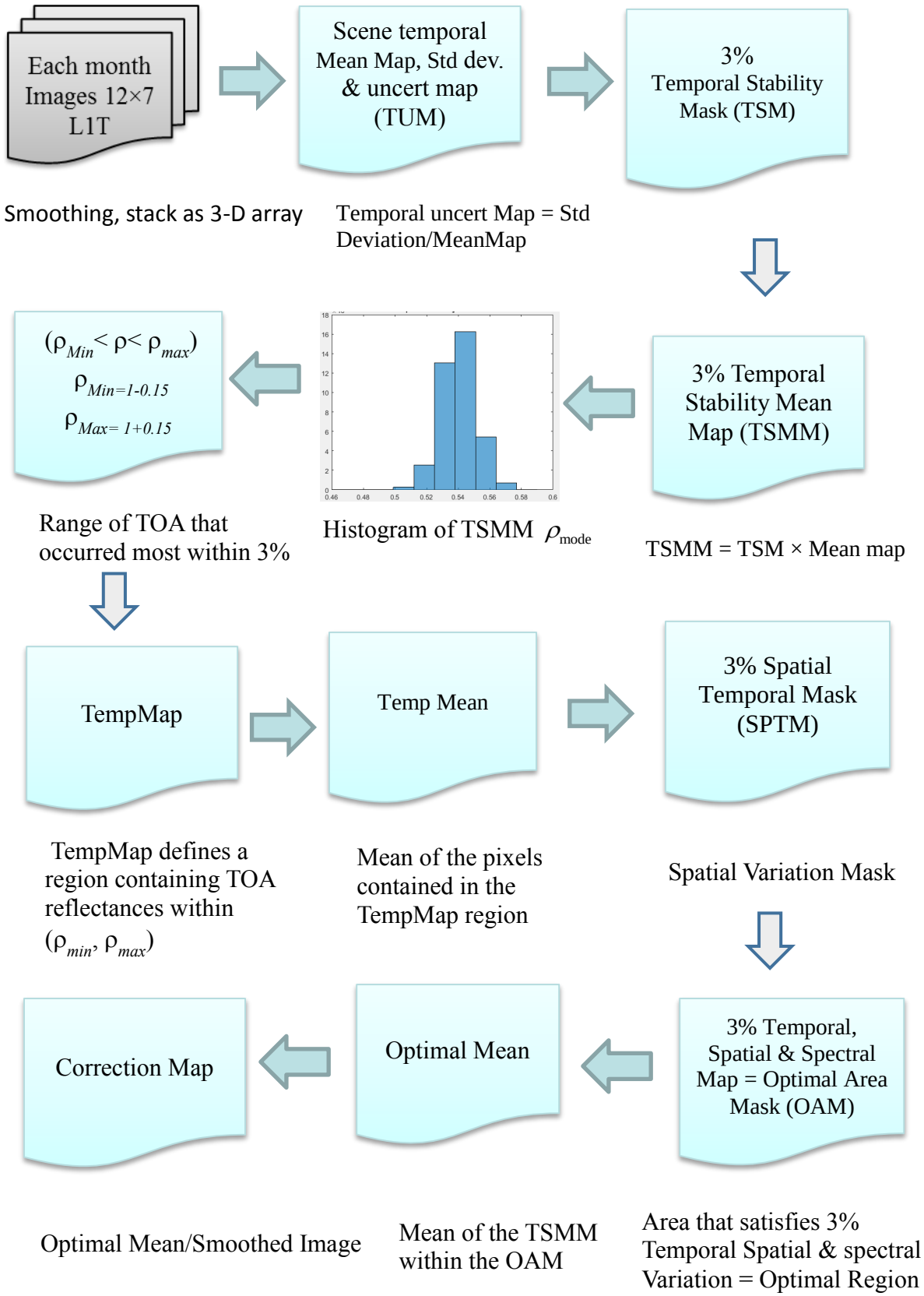

Figure 3.7. Processing flowchart for Normalization of Data from a Given PICS.

3.1.3 Normalization of Data across Multiple PICS:

Once the within-site normalization procedure described in Section 3.1.2 is completed, the variability in response for a single PICS is reduced by applying correction maps to bring all the pixel TOA reflectance levels to an optimal mean TOA reflectance for each PICS by reducing seasonal variability within each PICS. However, comparison of responses between PICS will still likely show significant differences in level. A second normalization procedure is then used to adjust the response of the PICS to achieve consistency with the Libya-4 reference as previously mentioned. The steps comprising this normalization procedure are described as follows. As with the previous normalization procedure, each band is processed separately. The essential part of this normalization procedure is to create "BaseMaps" which convert the TOA reflectance levels of multiple PICS to the selected reference TOA reflectance level.

1. For each non Libya-4 PICS, calculate a scaling factor defined as the ratio of the Optimal Reference value obtained for Libya-4 to the Optimal Reference value obtained for each PICS. The Optimal Reference values were obtained in Step 11 of the previous normalization stage.

$$SF = \frac{Optimal\ Reference(Libya-4)}{Optimal\ Reference(PICS)} \tag{13}$$

2. Create the set of monthly "BaseMaps" for each PICS by multiplying the scaling factor calculated in step 1 by the monthly correction maps determined in step 12 of the previous normalization stage:

$$Basemap(i,j,t) = CorrectionMap(i,j,t) \times SF \tag{14}$$

Figure 3.8 shows a summary of the across-PICS normalization procedure.

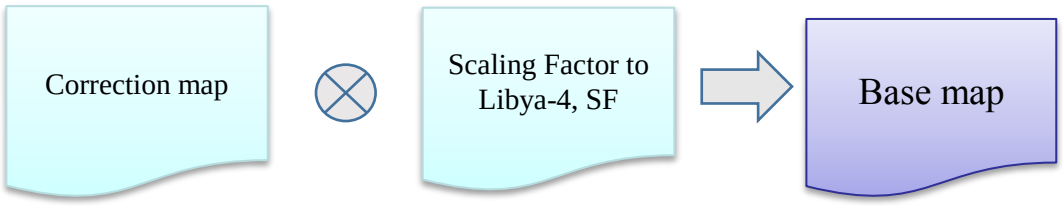

Figure 3.8. Flow chart for normalization across multiple PICS.

Once the monthly BaseMaps are calculated, they are applied to the original, cloud-free L1T image to create a PNP image normalized to Libya-4. The overall temporal mean, temporal standard deviation, and corresponding uncertainty are then calculated for the selected ROI within the scaled PNP image as described in Table 3.1. Figure 3.9 shows the final PNP processing prior to trending analysis.

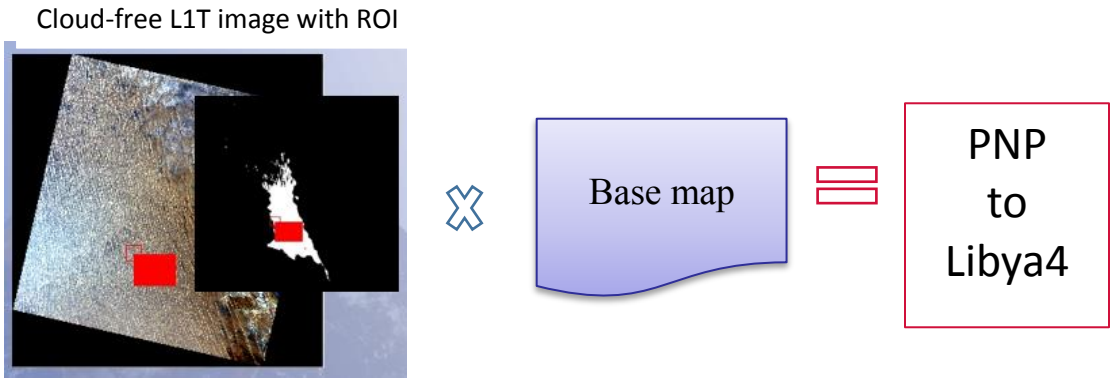

Figure 3.9. Flow chart for PICS Normalization.

The normalized PICS data obtained from the procedure described in Sections 3.1.2 and 3.1.3 are then combined into a single time-series dataset, creating a 'Super PICS'. In addition to estimating the uncertainties for each PICS, the temporal mean, temporal standard deviation, and uncertainty for the Super PICS dataset are calculated. From these summary statistical data, the overall uncertainty and the percentage drift for each PICS are estimated.

3.1.4 PNP Drift Estimates for OLI:

To reduce residual "noise" associated with measurement uncertainties for the individual PICS, the estimated drifts are inversely weighted by their uncertainties to derive a weighted average drift using equations (15) and (16). The weighting takes into account the difference of the mean drift derived from different sites as well as the number of observations from each of the PICS. These results will be presented in Chapter 4.

For N measurements $x_1, x_2, \ldots, x_N$ with uncertainties $\sigma_1, \sigma_2, \ldots, \sigma_N$ the weighted average is calculated as $\hat{y} = \frac{\sum_1^N W_i x_i}{\sum_1^N W_i}$ (15) [19]

where $w_i = \frac{1}{\sigma_i^2}$ and x_i is the % drift for each PICS and $\hat{y}$ is the weighted average drift. Typically when a mean is calculated, it is important to know the variance and standard deviation about that mean. when a weighted mean is used, the variance of the weighted sample is different from the variance of the unweighted sample.

$$\sigma = \sqrt{\frac{\sum n_i \sigma_i^2 + \sum n_i (\hat{y}_i - \hat{y})^2}{\sum n_i}} \quad (16) [19]$$

where $\hat{y}_i$ is the % drift for each PICS, n_i is the number of observations and σ is uncertainty.

3.2 Refined PICS Normalization Process (BRDF PNP):

The initial PICS normalization process as defined in the previous sections shows that the statistical drift didn't really match with the on-board calibrators because of the seasonal variations due to BRDF effects. An additional analysis was required in order to generate a reasonable BRDF model to improve the results. A separate processing procedure was

implemented in order to provide sufficient BRDF correction. The processing steps in the refined PICS normalization process are presented in Sections 3.2.2 and 3.2.3.

3.2.1 BRDF Overview:

Seasonal variation of TOA reflectance of a PICS target due to solar zenith angle can be particularly noticeable, especially in the longer wavelength bands. Several factors can affect this variability, including seasonal atmospheric aerosol/water vapor changes; the most significant contributor to this seasonal variation is BRDF effects [20] [21]. The Landsat series sensors, including OLI, are typically oriented for near- or at-nadir viewing; any BRDF effects arising from the sensor viewing geometry should be minimal. The solar zenith angle (SZA), however, varies considerably throughout the year. As a result, BRDF is most widely believed to be due to changes in illumination geometry induced by the variation in solar zenith angles. As discussed in Chapter 2, a linear BRDF model has often used to correct for BRDF effects [6] [10].

For his MS thesis, Shrestha [22] characterized BRDF using data acquired in the Algodones dunes PICS located near the United States-Mexico border. Two characterization methods were performed – one used surface radiance/reflectance data obtained during a 2015 field campaign, and the other performed laboratory measurements of sand samples obtained from various locations among the dunes during the same field campaign. The goal was to determine the most appropriate order for the model. Using linear regression analysis techniques, Shrestha discovered that linear and cubic terms were not statistically significant to a BRDF model, but the quadratic term was. All laboratory measurements were taken for solar zenith angle of 54.4˚and 45˚ which were

within the typical range of solar zenith and view angles were varied form +30˚ to -30˚. Based on these results, it can be reasonably concluded that the BRDF model applicable to PICS data is quadratic in nature. Consequently, a refined PNP procedure assuming a quadratic BRDF correction was developed. The refined procedure is presented in the following Sections. As currently implemented, the refined procedure is to be run AFTER the initial PNP procedure, as it relies on the previously selected ROIs and the original set of monthly smoothed image data.

3.2.2 Normalization of Data for an Individual PICS: Refined PNP

The following steps are used to create a set of monthly BRDF correction maps. As with the initial PNP procedure, each band is processed separately.

1. Derive the BRDF models as quadratic functions of the solar zenith angle and TOA reflectance. The input data for the models consist of the mean TOA reflectance within the ROI's selected during the initial PNP procedure; three years of data were used in the modeling. The solar zenith angles are time-dependent.
2. Calculate the BRDF correction factor corresponding to a solar zenith angle reference of 0° according to equation (17).

$$I'_{ref}(i,j) = p_1 \times {SZ_{ref}}^2 + p_2 \times SZ_{ref} + p_3 \quad (17)$$

3. Apply BRDF correction to the monthly smoothed images generated in step 1 of the initial PNP procedure: where SZ is the solar zenith angle of each selected image for corresponding PICS. $I''(i,j,t) = \frac{I'(i,j,t) \times {I'}_{ref}(i,j)}{p_1 \times SZ(i,j,t)^2 + p_2 \times SZ(i,j,t) + p_3}$ (18)
4. Stack the BRDF corrected images in temporal order as a 3D array and calculate the temporal mean image: $\mu(i,j) = \frac{1}{12}\sum_{t=1}^{12} I''(i,j,t)$ (19)

5. Use the selected ROI's OAM mask (red rectangles shown in Figure 3.5) determined from the initial PNP procedure to create an ORM image as indicated in equation (20), then calculate the Optimal Reference Mean value from the ORM image according to equation (21). The 'k' subscript in equation (21) indicates those ORM pixels with a nonzero value.

$$ORM^{BRDF} = OAM(i,j) \times \mu(i,j) \tag{20}$$

$$OptimalReference^{BRDF} = \frac{1}{N}\sum_{k=1}^{N} ORM_k{}^{BRDF} \tag{21}$$

6. With the calculated optimal reference mean value, generate monthly BRDF based correction maps using equation (22):

$$CorrectionMap(i,j,t)^{BRDF} = \frac{OptimalReference^{BRDF}}{I''(i,j,t)} \tag{22}$$

Figure 3.10 shows the processing flow for the refined procedure. BRDF correction is performed on each smoothed monthly image, and the corrected images are stacked in temporal order. Using the ROI OAM mask, the BRDF-corrected optimal region mean is calculated. The final correction maps are obtained by ratioing the BRDF optimal region mean and the monthly BRDF corrected images.

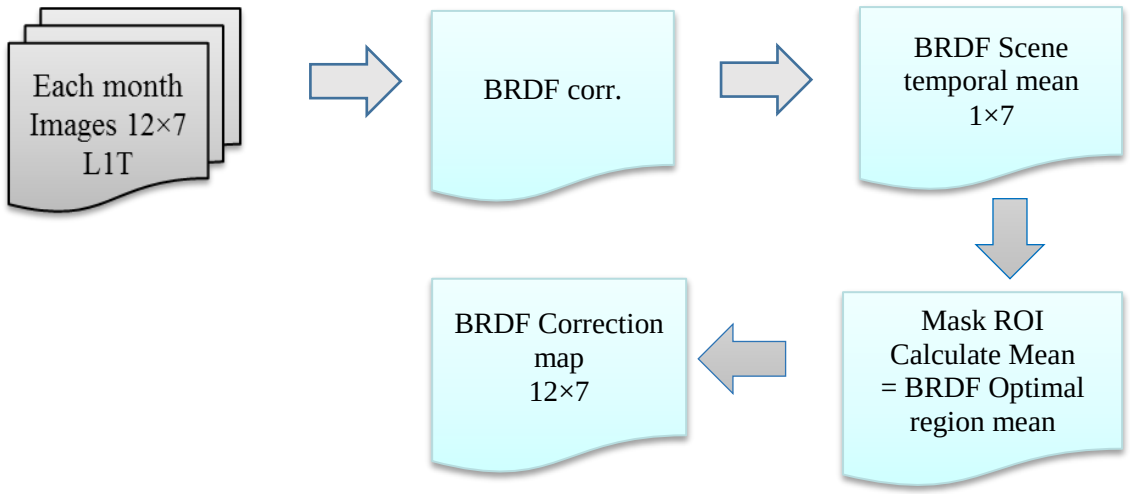

Figure 3.10. Flow chart for BRDF corrected normalization within PICS.

3.2.3 Normalization of data across Multiple PICS: Refined PNP

The steps comprising this cross-PICS normalization are described as follows. As with the previous PNP process, each band is processed separately.

1. For each non-Libya-4 PICS, calculate a BRDF corrected scaling factor defined as the ratio of the (BRDF corrected) Optimal Reference value obtained for Libya-4 to the (BRDF corrected) Optimal Reference value obtained for the PICS under consideration. The BRDF corrected Optimal Reference values were obtained in Step 5 (equation 21) of the previous normalization stage.

$$SF^{BRDF} = \frac{OptimalReference^{BRDF}(Libya{-}4)}{OptimalReference^{BRDF}(PICS)} \tag{23}$$

2. Create the set of monthly BRDF corrected BaseMaps for each PICS by multiplying the scaling factor calculated using equation (23) and the monthly correction maps determined in step 6 of Section 3.2.2:

$$Basemap^{BRDF}(i,j,t) = CorrectionMap^{BRDF}(i,j,t) \times SF^{BRDF} \tag{24}$$

Figure 3.11 shows the processing flow required to create the BRDF corrected BaseMap. This processing flow is identical to the cross-PICS normalization processing flow in the initial PNP procedure.

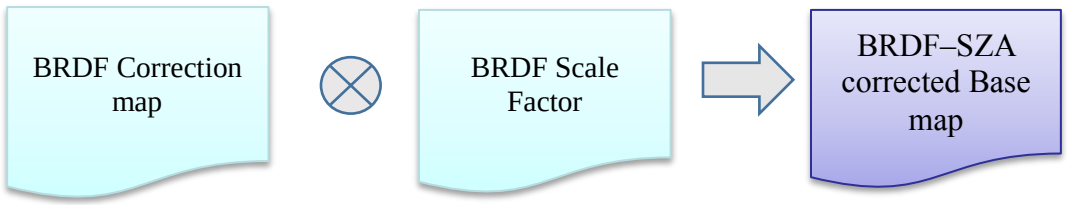

Figure 3.11. Flow chart for BRDF corrected normalization across PICS.

Once the BRDF corrected BaseMaps are created, they are applied to the cloud-free BRDF corrected L1T image data to create BRDF corrected PNP images normalized to Libya-4. The temporal mean, temporal standard deviation, and corresponding uncertainty are then calculated for the selected ROI within the BRDF corrected PNP image for individual PICS. Figure 3.12 shows the final BRDF corrected PNP processing prior to trending analysis.

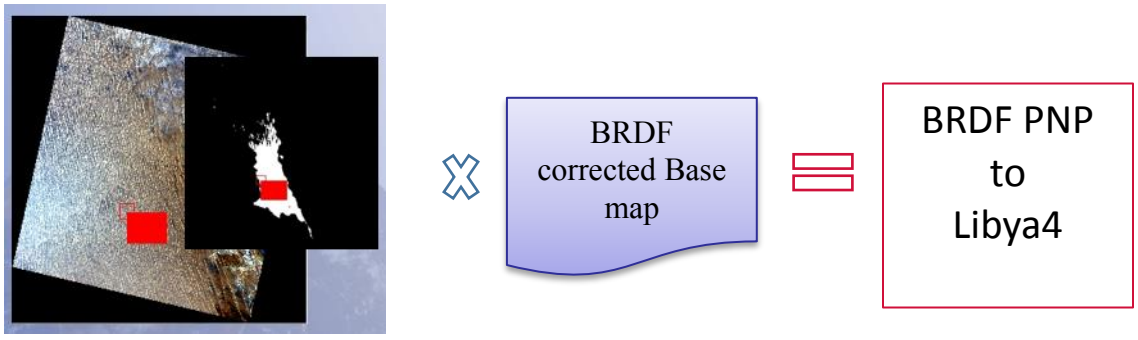

Figure 3.12. Flow chart for BRDF corrected PICS Normalization.

As with the initial PNP technique, the normalized PICS data obtained from the procedure described in Sections 3.2.2 and 3.2.3 are then combined into a single time-series dataset, creating a BRDF corrected Super PICS. In addition to estimating the overall uncertainties for each PICS, summary statistics for the BRDF corrected Super PICS are calculated.

3.2.4 BRDF corrected PNP Drift Estimates for OLI:

The same procedure shown in Section 3.1.4 is repeated for the BRDF corrected dataset. The results for this Section is also shown in Chapter 4.

3.3 BRDF corrected PNP Uncertainty Analysis:

There are two primary sources for uncertainty in the estimates generated from the BRDF corrected PNP technique:

1. Inherent uncertainty in the image data itself.
2. Uncertainty due to processing.

Both sources are considered in this Section.

3.3.1 Uncertainty in Image data:

OLI has stringent radiometric performance requirements. It is required to produce data calibrated to an uncertainty of less than five percent in terms of absolute, at-aperture spectral radiance and to an uncertainty of less than three percent in terms of TOA spectral reflectance for each of the spectral bands [2]. The inherent uncertainty in the image data for each band ($u_{inherent}$) is estimated by taking the average of the temporal uncertainties (u) derived for all the selected PICS:

$$u_{inherent} = \frac{1}{6}\sum_{i=1}^{6} u_i \tag{25}$$

3.3.2 Uncertainty due to Processing:

Each processing step in the BRDF corrected PNP technique will introduce a degree of uncertainty impacting the final results. The amount of uncertainty is a measure of sensitivity within the process.

The major contribution to the processing uncertainty within each PICS comes from calculating the temporal mean. Recall from Section 3.1.2 that the temporal mean is based

on a histogram analysis of the most commonly occurring TOA reflectances within the 3% range. Changing the number of bins can affect the histogram mode, which in turn affects the size of the range. If the range is too large then the accuracy of finding the most commonly occurring TOA reflectance level may change. Figure 3.13 shows the histograms resulting from selecting 10 vs 20 bins; with 10 bins the TOA reflectance ranged from 0.229 to 0.242, and with 20 bins the TOA reflectance ranged from 0.2377 to 0.2438. Changing the number of bins shifts the range of TOA reflectance levels. As a result, variation in the number of bins used in the histogram will produce uncertainty in the estimated temporal mean.

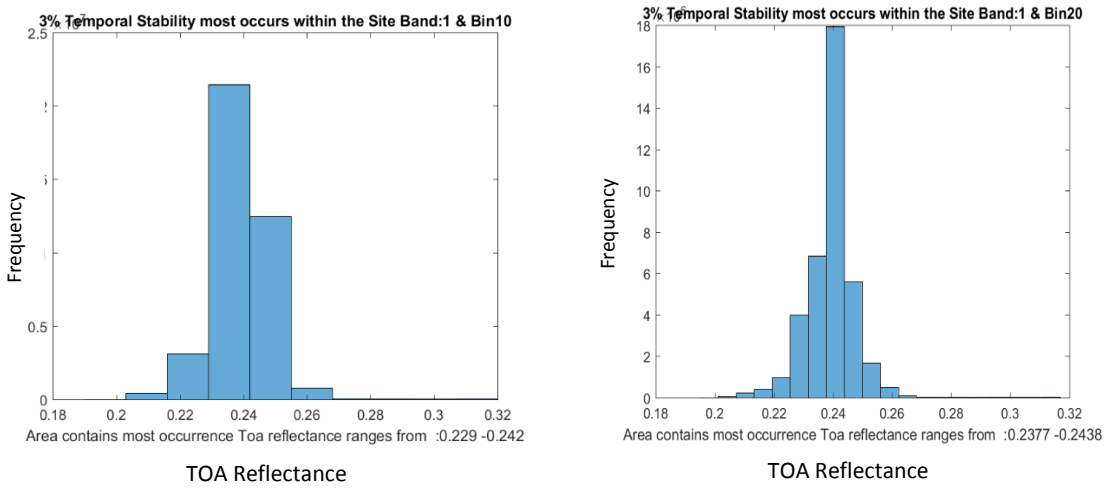

Figure 3.13. Histogram of temporal stability map for band 1 Libya-4 PICS using 10 bins (Left histogram) vs 20 bins (Right histogram).

Uncertainty in the temporal mean will lead to uncertainty in the optimal mean value, which will in turn lead to uncertainty in the correction map and corresponding scale factor calculation. These uncertainties will create uncertainty in the BaseMap and lead to uncertainty in the BRDF PNP results. A sensitivity analysis to quantify the amount of uncertainty in the BRDF PNP results was performed on the BRDF corrected image data

to determine the "best" number of bins to use in performing the histogram when calculating the temporal mean. Then, the temporal means resulting in each bin analysis were compared to the BRDF temporal mean. A brief description of the analysis is given below.

The number of histogram bins is set at 10, 15, 20, and 30. Histograms are generated with the selected number of bins, and the resulting optimal means are calculated. The results of this analysis suggest that the number of bins producing the "best" optimal mean estimate varies by site. The optimal mean value used for the BRDF corrected PNP technique is compared to the optimal means calculated from the sensitivity analysis. From this comparison, it was observed that the difference is within 1% for all bands and all PICS for each histogram bin number. For the calculation of sensitivity analysis uncertainty($u_{sensitivity}$), the "worst-case scenario" (highest difference to the initial BRDF optimal mean) was chosen for uncertainty analysis. The overall process uncertainty for each band is then calculated by temporally averaging the worst-case scenario uncertainty values for the "worst-case bin analysis" across 6 PICS.

The temporal uncertainty for the BRDF Super PICS ($u_{BRDF\ Super\ PICS}$) dataset is determined from the combined temporal trending data for the individual PICS.

The sensitivity analysis and BRDF Super PICS uncertainties are then combined with the inherent temporal image data uncertainty, calculated with equation (25), to obtain a final uncertainty given in equation (26):

$$U = \sqrt{(u_{inherent})^2 + (u_{sensitivity})^2 + (u_{BRDF\ Super\ PICS})^2} \tag{26}$$

The results of the Refined PNP uncertainty analysis will be presented in Chapter 4.

CHAPTER 4

RESULTS

4.1 PICS Normalization Process:

This Section presents the results obtained from the initial PNP normalization procedure described in Sections 3.1.1 and 3.1.2.

4.1.1 Normalization of Data for an Individual PICS:

As discussed in Chapter 3, pixel values from each PICS were normalized to the Optimal TOA Reflectance level (i.e. reflectance level representing an optimal area mask exhibiting 3% or less temporal, spatial, and spectral stability). The optimal area mask (OAM) for each PICS is indicated in Figures 4.1 – 4.6, represented as the area(s) in magenta. The areas in cyan represent the portions of the site not considered to be stable in any sense. The following Sections provide a brief description of the optimal area mask and the overall characteristics of each PICS. Descriptions of each PICS are based on summary descriptions for the site given in the USGS Remote Sensing Technologies Test Site Catalog [23].

Libya-1 (WRS2 path/row 187/043):

Figure 4.1 shows the true-color image and the identified optimal area mask of Libya-1 PICS. The surfaces at the site show a range of colors, from reddish-brown in the northwest corner, a lighter brown to tan color in the center, an off-white to whitish color in the southwest corner, and a blue to bluish-gray to slate color to the east and south. Dunes at the site also vary, with smaller dunes occurring at the northwestern corner of the site, to

longer and narrower dunes in the center; the eastern portions of the site appear to contain few if any dunes. The optimal area mask for this PICS (Figure 4.1) runs in a belt from southwest to northeast, between the west-central and north-central portions of the site, covering between one quarter to one third of the site. Smaller gaps in the area are observed towards the west, and a significant "fork" can be seen to the northeast. The OAM region does not appear especially homogeneous in the true-color image, as it is located in the areas containing the longer and narrower dunes.

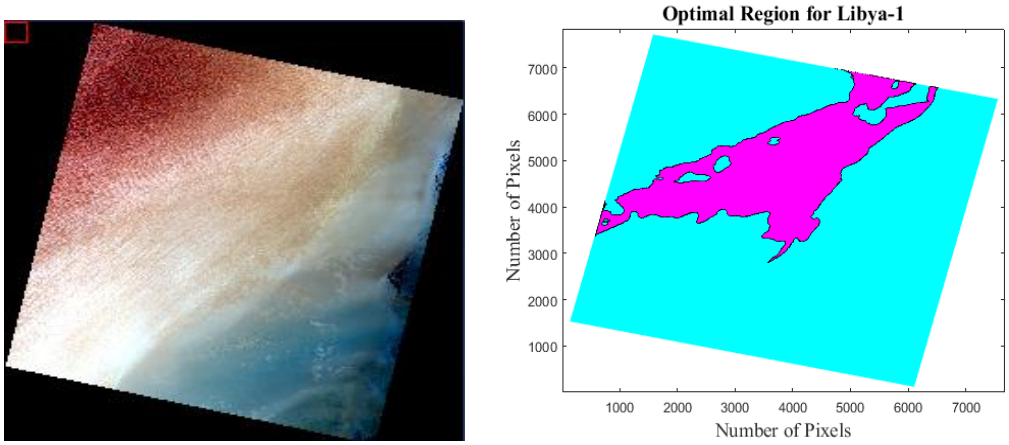

(a) Libya-1 True Color Image (b) Libya-1 Optimal Area Mask

Figure 4.1. Libya-1 True Color Image and Corresponding OAM.

Sudan-1 (WRS2 path/row 177/045):

Figure 4.2 shows the true-color image and the identified optimal area mask of Sudan-1 PICS. The surfaces at this site appear to be multi-colored in the true-color image, with more apparent variability than is seen in Libya-1. Some of the coloring in the extreme southeast suggests the presence of thin vegetation cover. Evidence of human agricultural practices can be seen in the far north, with the presence of areas of circular irrigation of crop land. The corresponding OAM generally runs in a belt from west to east across most

of the site, with most of the region concentrated in the south. There are more gaps and "holes" in the region than is observed for Libya-1. The OAM region appears to be more homogeneous than is observed in Libya-1, consisting primarily of bluish-gray to slate colored sands as seen in the true-color image.

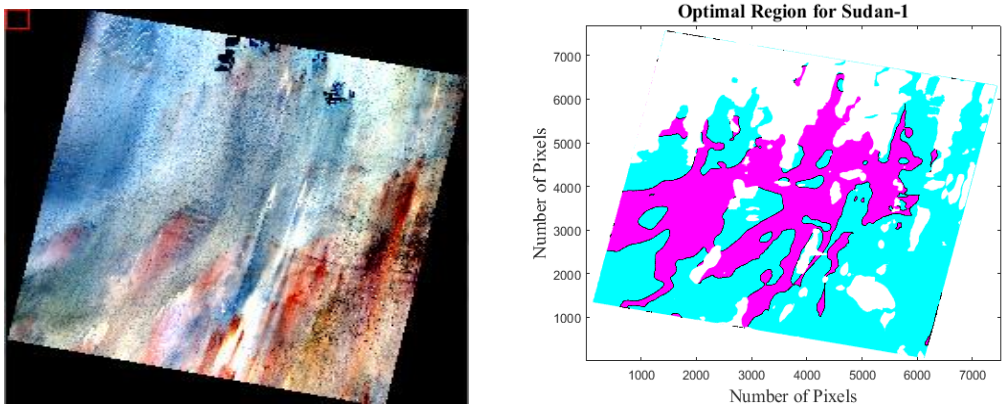

(a) Sudan-1 True Color Image (b) Sudan-1 Optimal Area Mask

Figure 4.2. Sudan-1 True Color Image and Corresponding OAM.

Niger-1 (WRS2 path/row 189/046):

Figure 4.3 shows the true-color image and the identified optimal area mask of Niger-1 PICS. The surfaces in the west appear as darker shades of grayish-blue to dark brown to black in the true-color image. These surfaces are may be a rock's. The OAM for this PICS lies roughly within the east-central portion of the site, with the area roughly equally divided between north and south. The sands appear to be most homogeneous in character in these parts of the site, generally a light brown to tan to off-white in color as seen in the true color image, with almost no dunes observed in the area. There are multiple, smaller optimal "sub-regions" not physically connected to the main region, mainly occurring towards the west and south.

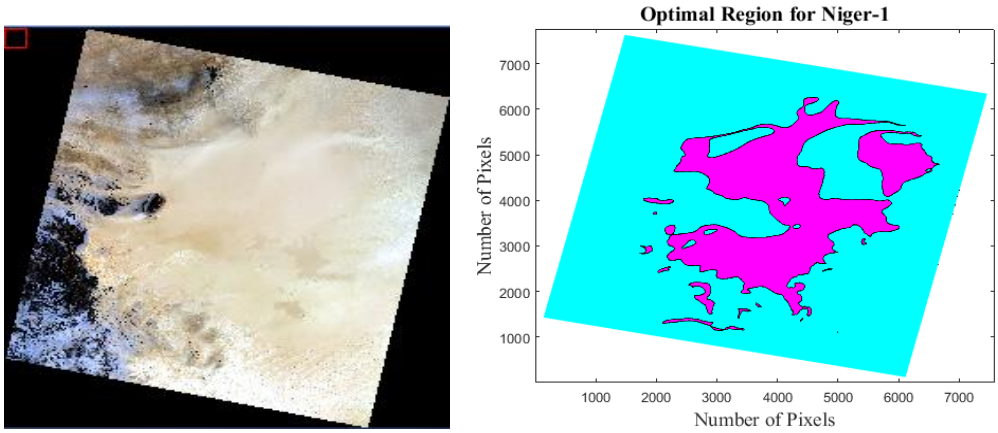

(a) Niger-1 True Color Image (b) Niger-1 Optimal Area Mask

Figure 4.3. Niger-1 True Color Image and Corresponding OAM.

Egypt-1 (WRS2 path/row 179/041):

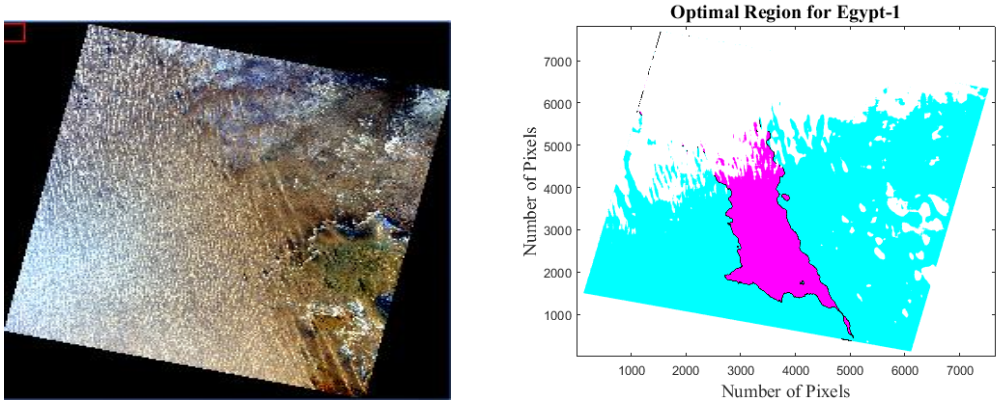

(a) Egypt-1 True Color Image (b) Egypt-1 Optimal Area Mask

Figure 4.4. Egypt-1 True Color Image and Corresponding OAM.

Figure 4.4 shows the true-color image and the identified optimal area mask of Egypt-1 PICS. As seen in the true color image, the surfaces at the site are a mix of sands and rocks, with sands to the west and south, and rocks to the southeast and north. The sands appear to be brownish in color and show evidence of long, narrow dunes concentrated in the west and east-central portions of the site. The optimal area mask for this PICS lies in a belt within the south-central portion of the site, running from northwest to southeast, with

most of the region concentrated in the south. The OAM appears to be in the most homogeneous part of the site where the sands are lighter brown in color with narrower dunes.

Niger-2 (WRS2 path/row 188/045):

Figure 4.5 shows the true-color image and the identified optimal area mask of Niger-2 PICS. The surfaces in the south and west appear to be very homogeneous, appearing to be a mix of tan, off-white, and gray-colored sands. A ridge running from southeast to northwest can be seen, showing a transition to a rockier, less sandy area in the northeast. The optimal area mask for this PICS runs in a belt from the extreme south-central to southwestern portions of the site. It consists of two main areas connected by a narrow strip. Multiple smaller optimal sub-regions can be seen in the east, and a single optimal sub-region can be seen to the north. The OAM is primarily in the homogeneous region with the tan to grey colored sands.

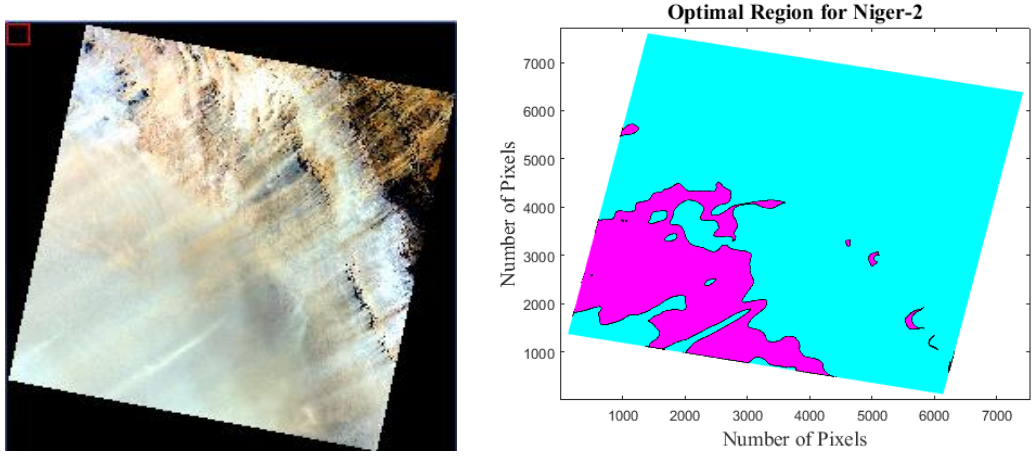

(a) Niger-2 True Color Image (b) Niger-2 Optimal Area Mask

Figure 4.5. Niger-2 True Color Image and Corresponding OAM.

Libya-4 (WRS2 path/row 181/040):

Figure 4.6 shows the true-color image and the identified OAM of Libya-4 PICS. The surfaces at the site are predominantly brown to tan colored sand. A rockier area appearing dark blue with areas of white can be seen in the far north. Dunes of varying lengths and widths can be seen in nearly all of the true color image; the dunes appear to be longer and deeper towards the south and east. The region defining the OAM for this PICS is by far the largest among the selected PICS used in this thesis work. The main area of the region covers more than 50% of the site, running across nearly all of the site to the north. The OAM region narrows considerably to the south, where it is primarily in the west-central portion of the site. Multiple smaller regions can be seen near the main part of the region, primarily to the south and east; a single sub-region band can be seen in the far northeast. The OAM lies in the sandier parts of the site with fewer significant dunes.

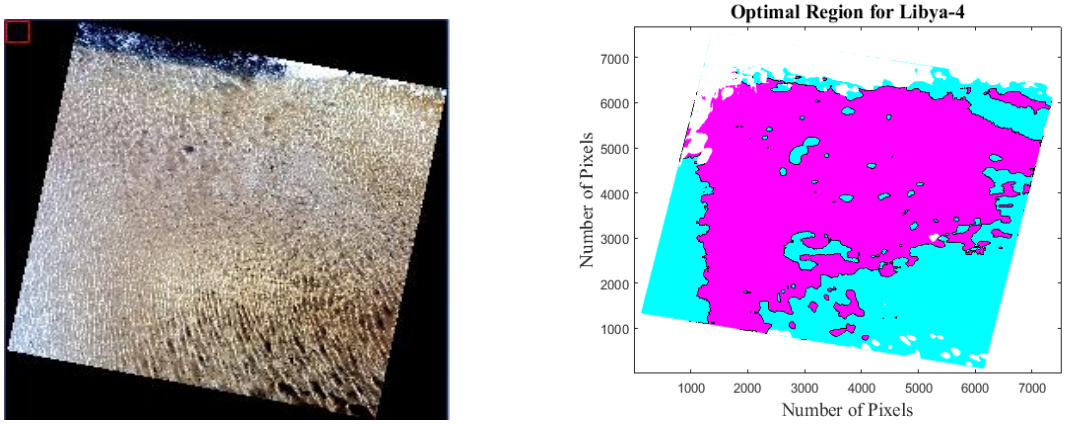

(a) Libya-4 True Color Image (b) Libya-4 Optimal Area Mask

Figure 4.6. Libya-4 True Color Image and Corresponding OAM.

Following the procedure described in Section 3.1.2 and described in equation (11), the optimal mean TOA reflectance is calculated for each band at each site. Table 4.1 shows the results of these calculations.

As indicated in Section 3.1.2, these values normalize the TOA reflectance levels in an image to the TOA reflectance level determined to optimally represent the site; the optimal mean value is band and site dependent, primarily due to the characteristics of the material(s) comprising the site as described in Section 4.1.1. Once the optimal mean values were calculated, the correction maps for each month were then calculated according to equation (12).

Normalization within the PICS – Optimal mean Values of Different PICS						
Band	**Egypt-1**	**Sudan-1**	**Niger-1**	**Niger-2**	**Libya-1**	**Libya-4**
C/A	0.2144	0.2093	0.1972	0.2000	0.1895	0.2289
Blue	0.2274	0.2184	0.2113	0.2060	0.2040	0.2470
Green	0.314	0.3009	0.3134	0.2790	0.3070	0.3329
Red	0.4275	0.4319	0.4644	0.3960	0.4910	0.4520
NIR	0.5561	0.5405	0.5831	0.4960	0.6170	0.5771
SWIR1	0.676	0.6646	0.6976	0.6370	0.7150	0.6697
SWIR2	0.5881	0.5784	0.6118	0.5600	0.6130	0.5835

Table 4.1 PNP Optimal TOA reference for all 6 PICS and all 7 bands.

4.1.2 Normalization of Data across Multiple PICS:

As discussed in Section 3.1.3, scaling factors for all PICS are calculated according to equation (13), in order to normalize them to the Libya-4 optimal mean value. Table 4.2 shows the results of these calculations. As expected, the scale factors for the non-Libya-4 PICS are very close to 1, and exactly 1 for Libya-4.

Normalization across PICS – Scale Factor Values						
Band	**Egypt-1**	**Sudan-1**	**Niger-1**	**Niger-2**	**Libya-1**	**Libya-4**
C/A	1.0676	1.0936	1.1608	1.1445	1.2079	1
Blue	1.0862	1.1310	1.1690	1.1990	1.2108	1
Green	1.0602	1.1063	1.0622	1.1932	1.0844	1
Red	1.0573	1.0465	0.9733	1.1414	0.9206	1
NIR	1.0378	1.0677	0.9897	1.1635	0.9353	1
SWIR1	0.9907	1.0077	0.9600	1.0513	0.9366	1
SWIR2	0.9922	1.0088	0.9537	1.0420	0.9519	1

Table 4.2 PNP Scale factor values for all 6 PICS of all 7 bands.

After applying the scale factor values to each selected PICS with corresponding correction maps, the BaseMaps are created. The significance of these BaseMaps is to bring each PICS optimal TOA reflectance level to the Libya-4 optimal TOA reflectance level. The PNP was then performed and trending analysis for each PICS was calculated. Figure 4.7 and Figure 4.8 shows the resulting TOA reflectances for all PICS after PNP.

With the exception of the Egypt-1 PICS, the remaining PICS TOA reflectances agree quite well with the PNP Libya-4 PICS TOA reflectances. Residual seasonal variation is observed in the Red and NIR bands as pointed out with red arrow. Figure 4.8 shows the TOA reflectance results for all PICS in the Coastal/Aerosol and SWIR2 bands. The observed values are in the same range as the corresponding TOA reflectances of the Blue and SWIR1 bands, respectively, and would have been difficult to visualize when plotted against those bands in Figure 4.7. For the Coastal/Aerosol band, the TOA reflectances of

all PICS are in very good agreement. For the SWIR2 band the agreement in TOA reflectances is worse, due to residual seasonal variation.

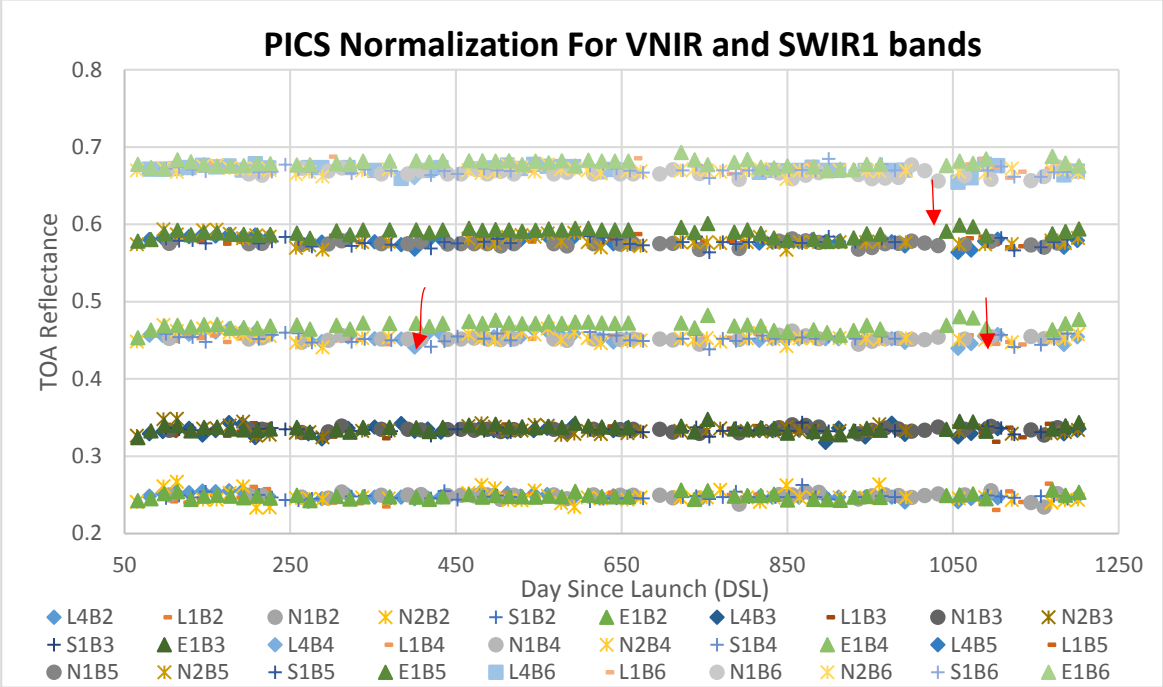

Figure 4.7. PNP Trending for 5 spectral bands of 6 PICS (VNIR and SWIR1).

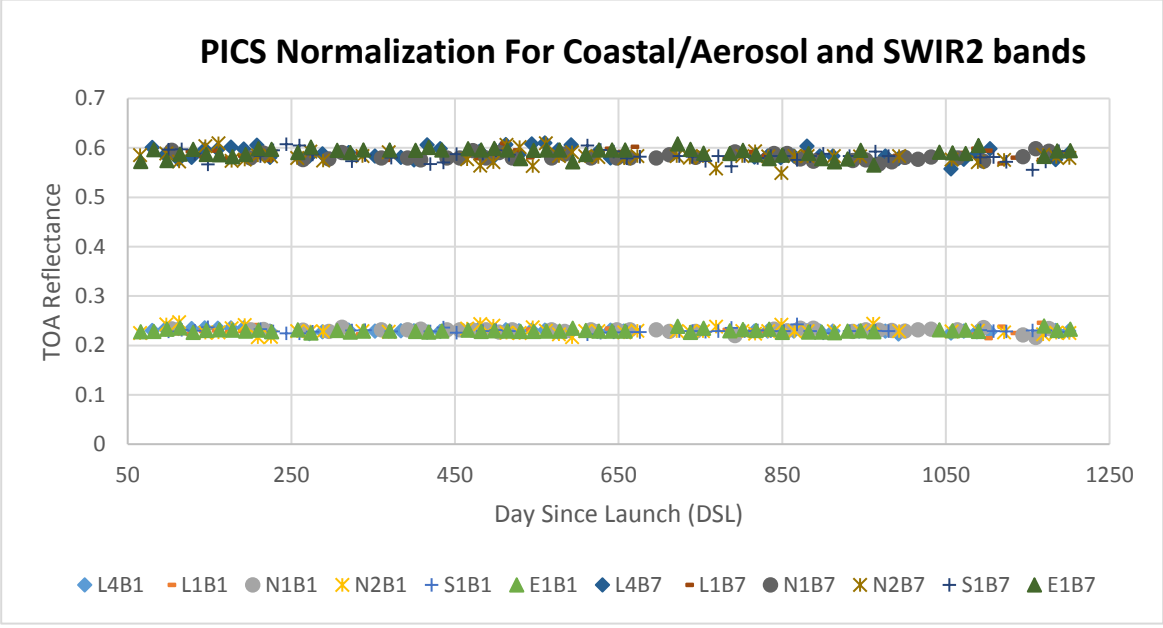

Figure 4.8. PNP Trending for 2 spectral bands of 6 PICS (Coastal/Aerosol and SWIR2).

After the PNP is applied to all of the archived images, temporal uncertainties are calculated for each PICS (temporal standard deviation/temporal mean). Table 4.3 shows the resulting temporal uncertainty estimates. Overall, the temporal uncertainty for most PICS is well within 2.5% for all spectral bands. The Libya-1 and Niger-2 PICS have slightly higher uncertainties in the C/A and Blue bands, on the order of 3%. The uncertainty in the SWIR2 band for Niger-2 was also slightly higher, but well within 2.5%.

PICS_PNP Uncertainty	C/A	Blue	Green	Red	NIR	SWIR1	SWIR2
Libya-4	1.22%	1.37%	1.39%	1.30%	0.93%	0.78%	1.90%
Libya-1	2.55%	2.65%	1.62%	0.82%	0.65%	0.83%	1.38%
Niger-1	1.74%	1.67%	0.86%	0.65%	0.50%	0.73%	1.75%
Niger-2	3.01%	3.11%	1.59%	1.33%	1.11%	0.51%	2.22%
Sudan-1	1.51%	1.45%	0.93%	1.10%	0.79%	0.69%	1.87%
Egypt-1	1.24%	1.33%	1.29%	1.16%	0.90%	0.65%	1.52%

Table 4.3 % temporal uncertainties for all 7 bands for each PICS after PNP trending.

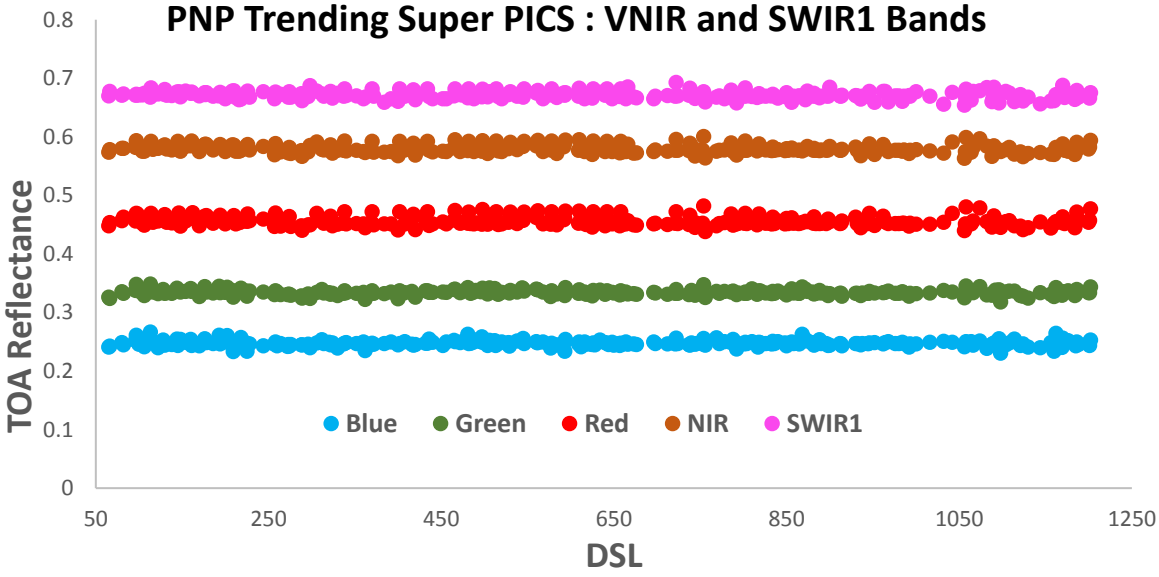

Figure 4.9. PNP Super PICS trending for VNIR and SWIR1 bands.

Figure 4.9 shows the TOA reflectance trend after combining 6 PICS into a Super PICS dataset in the Blue, Green, Red, NIR and SWIR1 bands with a total number of 320 images. A change in response can be seen in the 2016 data (approximately from DSL 1050 to 1200); the change is more noticeable for the longer wavelength bands. The major contribution to that change appears to come from the Egypt-1 PICS data, perhaps due to uncorrected BRDF effects, which can also clearly be seen in Figures 4.7 and 4.8.

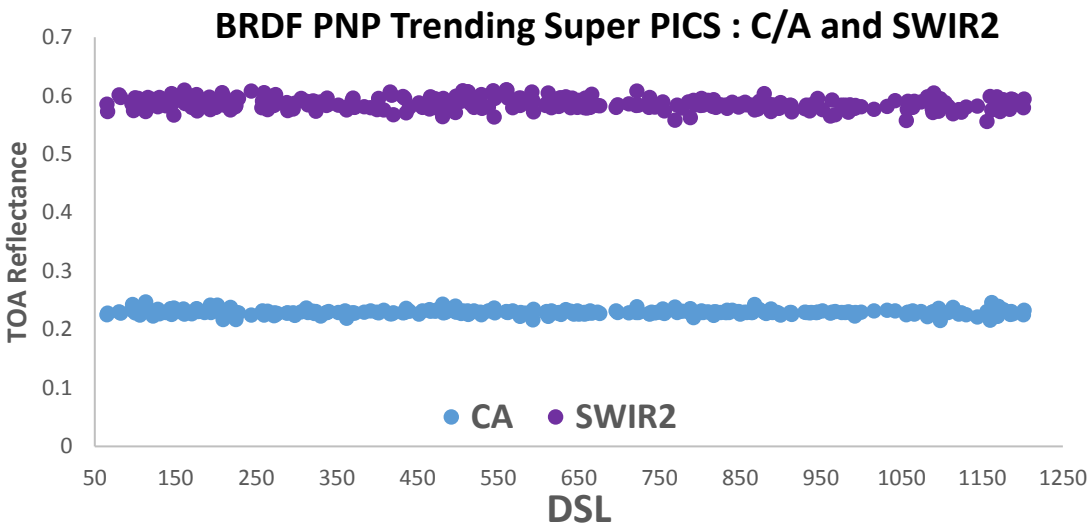

Figure 4.10. PNP Super PICS trending for Coastal/Aerosol and SWIR2 bands.

Figure 4.10 shows the Super PICS trending results for the Coastal/Aerosol and SWIR2 bands. The change in 2016 data appears to be less noticeable in these bands. For the Coastal/Aerosol band the overall variation is much less, while for the SWIR2 band the residual seasonal variation appears to be more dominant.

4.1.3 PNP Drift Estimates for OLI:

Gain drift in % per year is estimated from trending of individual PNP PICS data, the weighted average of the PNP PICS data and the combined Super PICS data. Table 4.4

gives the estimates for all PNP PICS along with the estimates for the weighted average and Super PICS dataset and Table 4.5 shows the corresponding 2-sigma uncertainties for each PICS.

The estimated drift is highest for Libya-4, with values greater than -0.5% per year for all spectral bands except SWIR1, which has an estimated drift on the order of -0.3%. Sudan-1 has the lowest estimated drifts, on the order of -0.2% per year, for all bands. The drift estimates for the other PNP PICS appear to be consistent with each other.

Percentage drift per year for PNP analysis								
PNP Drift	**Libya-4**	**Libya-1**	**Niger-1**	**Niger-2**	**Sudan-1**	**Egypt-1**	**W.avg**	**Super PICS**
C/A	-0.66	0.13	-0.56	-0.40	-0.23	0.21	-0.33	-0.24
Blue	-0.79	0.10	-0.34	-0.34	-0.15	0.32	-0.27	-0.19
Green	-0.72	-0.05	0.07	-0.40	-0.10	0.23	-0.14	-0.18
Red	-0.64	-0.08	0.12	-0.52	-0.12	0.15	-0.14	-0.28
NIR	-0.54	-0.06	-0.07	-0.47	-0.10	0.10	-0.18	-0.25
SWIR1	-0.27	-0.08	-0.34	-0.12	0.00	0.03	-0.16	-0.18
SWIR2	-0.62	-0.11	-0.09	-0.63	-0.21	-0.16	-0.45	-0.41

Table 4.4 Percentage drift per year for each PICS using PNP technique.

2 sigma values for PNP analysis								
PNP 2-sigma	**Libya-4**	**Libya-1**	**Niger-1**	**Niger-2**	**Sudan-1**	**Egypt-1**	**W.avg**	**Super PICS**
C/A	0.35	0.93	0.65	0.98	0.33	0.38	0.78	0.26
Blue	0.38	0.97	0.64	1.02	0.30	0.40	0.81	0.27
Green	0.38	0.59	0.34	0.51	0.21	0.39	0.54	0.18
Red	0.35	0.30	0.25	0.41	0.26	0.36	0.46	0.24
NIR	0.24	0.24	0.19	0.34	0.19	0.27	0.36	0.16
SWIR1	0.23	0.30	0.26	0.16	0.17	0.20	0.27	0.12
SWIR2	0.57	0.50	0.68	0.70	0.44	0.46	0.67	0.23

Table 4.5 2-Sigma values for each PICS using PNP technique.

The observed drifts for the PNP weighted average and Super PICS estimates are within -0.35% and -0.3% per year, respectively, for all bands except SWIR2 which has drift estimates of approximately -0.45% and -0.41% per year, respectively.

A statistical analysis is performed to test the zero slope hypothesis at the 95% confidence level for the Super PICS dataset. The significance of this analysis to estimate the drift of OLI sensor. For the longer wavelength bands there is sufficient statistical evidence to conclude non-zero slopes, especially for the NIR, SWIR1 and SWIR 2 bands; their p-values were significantly small. For the shorter wavelengths, only Coastal/Aerosol and Blue bands show the zero-slope with p-value is greater than 0.05. For all spectral bands except SWIR2 the estimated drift is less than -0.3% per year; for SWIR2, the estimated drift is within -0.45% per year. The corresponding temporal uncertainties in the estimates are within 2% for all spectral bands. Table 4.6 shows the results of this analysis.

PNP Super PICS	C/A	Blue	Green	Red	NIR	SWIR1	SWIR2
%Drift/year	-0.24	-0.19	-0.18	-0.28	-0.25	-0.18	-0.41
2Sigma	0.26	0.27	0.18	0.24	0.16	0.12	0.23
p-value Slope = 0	0.0682	0.1447	0.0436	0.023	0.0023	0.0048	0.0004
Uncertainty	1.91%	1.95%	1.33%	1.79%	1.19%	0.92%	1.73%

Table 4.6 PNP Super PICS Statistical analysis for the estimation of drift for OLI.

The analysis results presented so far apply to the initial PNP technique, in which no explicit BRDF corrections have been applied to the data. All normalizations performed in the initial technique could perhaps be considered a “pseudo” BRDF correction, as any BRDF effects would be largely averaged out. Performing explicit BRDF correction as part of PNP processing should improve the results. These results are presented in the following Sections. Figure 4.11 shows the combined plot of these estimates.

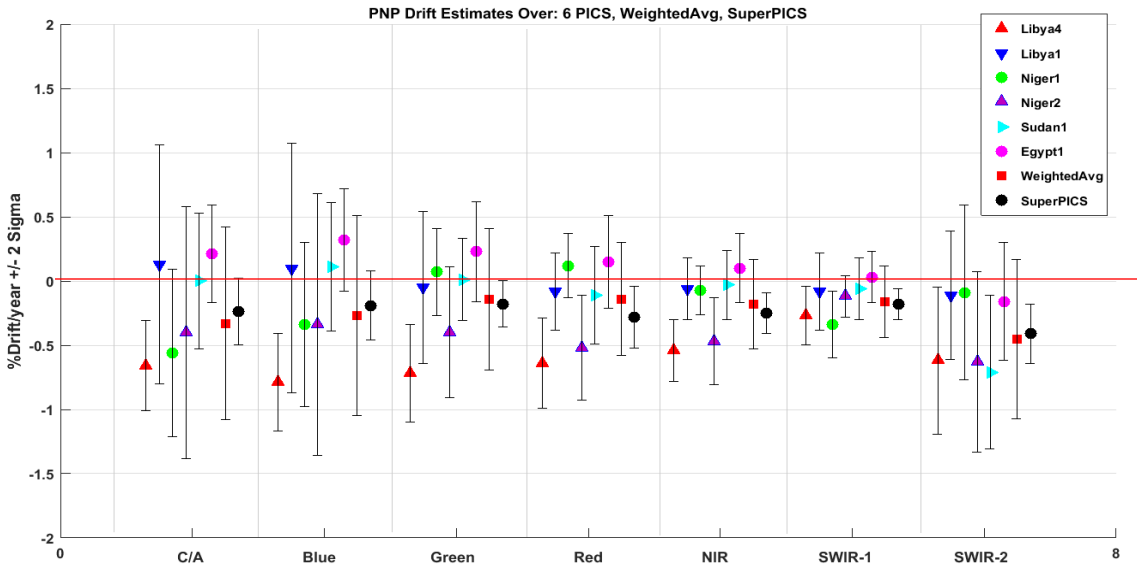

Figure 4.11. % Drift comparison for individual PNP PICS, weighted avg. & Super PICS.

4.2 Refined PICS Normalization Process:

This Section presents the results obtained for the BRDF corrected normalization technique described in Sections 3.2.1 and 3.2.2. As indicated in Chapter 3 quadratic BRDF models as functions of the solar zenith angles are generated for each PICS. Tables 4.7 through 4.12 show the resulting model coefficients for all 7 bands and all 6 PICS.

Egypt-1	P_1	P_2	P_3
C/A	1.599e-05	-0.0010580	0.2311
Blue	1.405e-05	-0.0009932	0.2449
Green	6.447e-06	-0.0005894	0.3305
Red	6.799e-06	-0.0008057	0.4645
NIR	1.027e-05	-0.0012350	0.5991
SWIR1	4.429e-06	-0.0013320	0.7278
SWIR2	2.214e-05	-0.0023770	0.6492

Table 4.7 BRDF Coefficients for Egypt-1 PICS ($f(x) = p_1*x^2 + p_2*x + p_3$).

Libya-1	P_1	P_2	P_3
C/A	9.219e-06	-0.0006889	0.1999
Blue	5.278e-06	-0.0004457	0.2109
Green	-3.303e-06	0.0001622	0.3060
Red	-1.013e-05	0.0003419	0.4908
NIR	-3.413e-06	-0.0005108	0.6357
SWIR1	-2.706e-06	-0.0012370	0.7583
SWIR2	-1.002e-05	-0.0001486	0.6321

Table 4.8 BRDF Coefficients for Libya-1 PICS ($f(x) = p_1*x^2 + p_2*x + p_3$).

Niger-1	P_1	P_2	P_3
C/A	3.024e-05	-0.0021250	0.2347
Blue	2.859e-05	-0.0019990	0.2468
Green	1.307e-05	-0.0008231	0.3267
Red	4.571-06	-0.0004162	0.4725
NIR	2.875e-06	-0.0006748	0.5983
SWIR1	-6.028e-06	-0.0010740	0.7331
SWIR2	1.652e-05	-0.0019650	0.6516

Table 4.9 BRDF Coefficients for Niger-1 PICS ($f(x) = p_1*x^2 + p_2*x + p_3$).

Niger-2	P_1	P_2	P_3
C/A	1.589e-05	-0.0012820	0.2240
Blue	1.663e-05	-0.0014120	0.2328
Green	1.260e-05	-0.0010560	0.2984
Red	9.994e-06	-0.0008829	0.4118
NIR	7.784e-06	-0.0009073	0.5153
SWIR1	-4.409e-07	-0.0008099	0.6624
SWIR2	2.217e-05	-0.0018220	0.5907

Table 4.10 BRDF Coefficients for Niger-2 PICS ($f(x) = p_1*x^2 + p_2*x + p_3$).

Sudan-1	P_1	P_2	P_3
C/A	6.026e-06	-0.0004665	0.2175
Blue	6.689e-06	-0.0006012	0.2295
Green	1.154e-05	-0.0010300	0.3192
Red	2.226e-05	-0.0020320	0.4679
NIR	1.732e-05	-0.0019480	0.5823
SWIR1	1.130e-05	-0.0020300	0.7256
SWIR2	5.831e-05	-0.0049610	0.6771

Table 4.11 BRDF Coefficients for Sudan-1 PICS ($f(x) = p_1*x^2 + p_2*x + p_3$).

OLI Band	p_1	p_2	p_3
C/A	1.433e-05	-9.290e-04	0.2404
Blue	1.351e-05	-9.513e-04	0.2620
Green	8.960e-06	-8.324e-04	0.3533
Red	1.174e-05	-0.001200	0.4866
NIR	1.228e-05	-0.001500	0.6164
SWIR1	7.016e-06	-0.001600	0.7213
SWIR2	4.655e-05	-0.004300	0.6818

Table 4.12 BRDF Coefficients for Libya-4 PICS. ($f(x) = p_1*x^2 + p_2*x + p_3$).

4.2.1 Refined PICS Normalization of Data for an Individual PICS:

BRDF corrected optimal mean values are generated from the ROIs selected in the initial PNP processing and the BRDF corrected temporal mean images, as shown in equations (17) through (19). The resulting optimal mean values for the individual PICS are shown in Table 4.13. These values bring all pixel TOA levels of site to an optimal TOA reflectance level.

4.2.2 Refined PICS Normalization of Data across Multiple PICS:

Table 4.14 gives the BRDF corrected scale factors determined from the BRDF corrected optimal mean values. As noted for the initial technique's scaling factors, the values for the Libya-4 PICS are exactly 1, while the remaining PICS have scaling factors close to 1. After creating BRDF corrected BaseMaps and performing BRDF PNP, a trending analysis similar to the initial PNP analysis was performed. Figure 4.12 shows the results of this analysis for the Blue, Green, Red, NIR, and SWIR1 bands. The overall trends indicate decreased variability due to BRDF effects. Variability in response to longer

wavelength bands is significantly reduced for the Egypt-1. However, residual seasonal variation is still apparent, especially during 2013 and 2014 (DSL 50 to DSL 650).

Normalization within PICS – BRDF Optimal mean Values of Different PICS						
Band	**Egypt-1**	**Sudan-1**	**Niger-1**	**Niger-2**	**Libya-1**	**Libya-4**
C/A	0.2312	0.2175	0.2334	0.2233	0.1997	0.2399
Blue	0.2449	0.2293	0.2455	0.2320	0.2106	0.2613
Green	0.3299	0.3181	0.3262	0.2978	0.3059	0.3521
Red	0.4633	0.4669	0.4720	0.4120	0.4899	0.4850
NIR	0.5979	0.5820	0.5967	0.5151	0.6338	0.6154
SWIR1	0.7273	0.7245	0.7312	0.6628	0.7544	0.7205
SWIR2	0.6482	0.6738	0.6526	0.5941	0.6293	0.6795

Table 4.13 BRDF PNP Optimal mean values for all 6 PICS and all 7 bands.

Normalization across PICS – Scale Factor Values						
Band	**Egypt-1**	**Sudan-1**	**Niger-1**	**Niger-2**	**Libya-1**	**Libya-4**
C/A	1.0377	1.1031	1.0281	1.0743	1.2018	1
Blue	1.0670	1.1395	1.0646	1.1262	1.2406	1
Green	1.0672	1.1068	1.0795	1.1823	1.1511	1
Red	1.0468	1.0386	1.0275	1.1771	0.9899	1
NIR	1.0293	1.0575	1.0313	1.1947	0.9711	1
SWIR1	0.9907	0.9945	0.9854	1.0871	0.9551	1
SWIR2	1.0483	1.0084	1.0412	1.1437	1.0797	1

Table 4.14 BRDF PNP per-band scaling factor values for 6 PICS and all 7 bands.

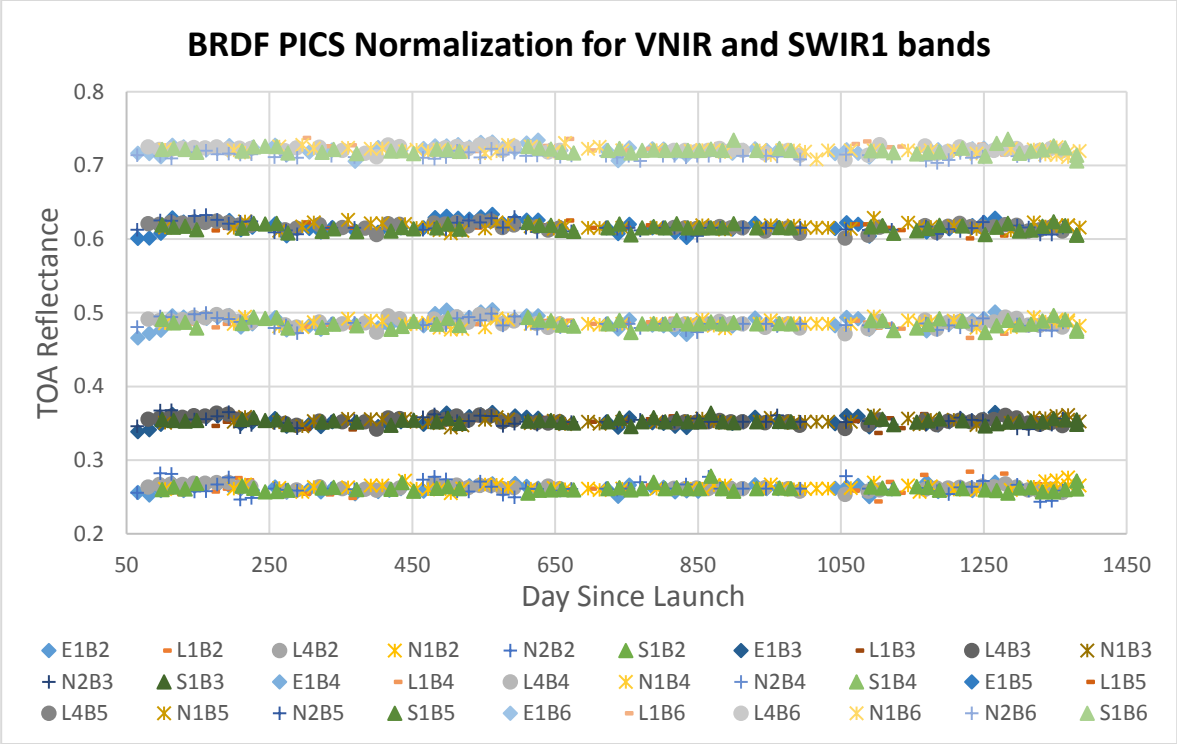

Figure 4.12. BRDF PNP Trending for 6 PICS (VNIR and SWIR1).

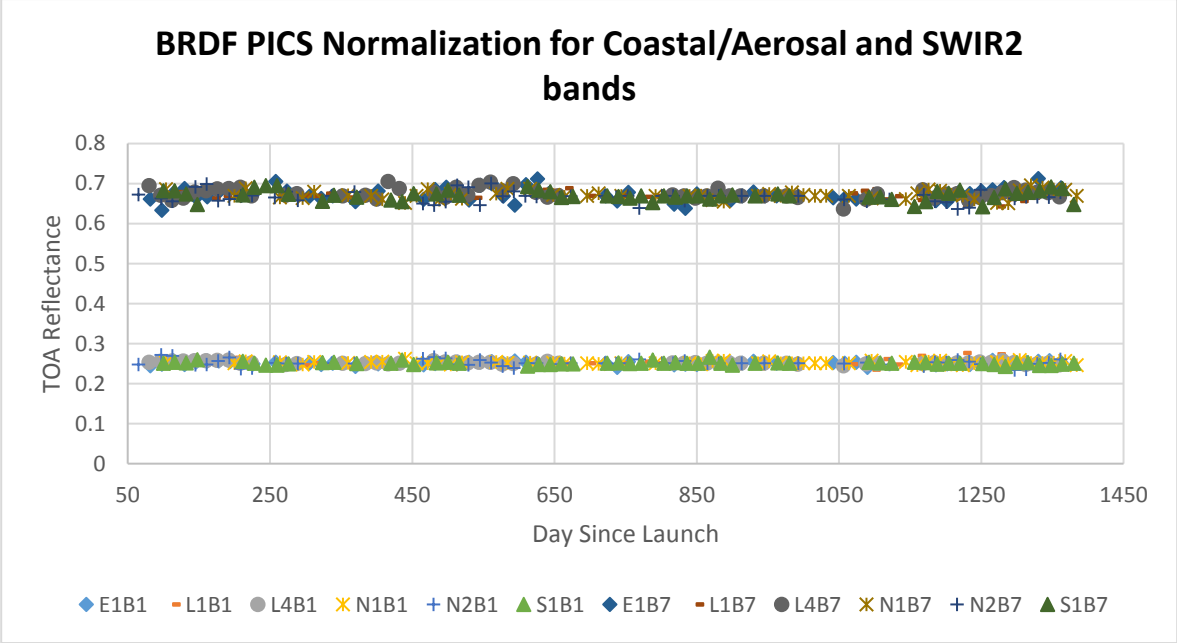

Figure 4.13. BRDF PNP Trending for 6 PICS (Coastal/Aerosol and SWIR2).

Figure 4.13 shows the corresponding trends for all PICS in the Coastal/Aerosol and SWIR2 bands. Overall variability appears to have been reduced; however, 2016 data from the Libya-1 PICS appears to be showing greater variability. This variability is most likely due to atmospheric aerosol effects during this period. As with the other bands, residual seasonal variation can be observed in the 2013 and 2014 data.

Once the BRDF normalization technique is completed, temporal uncertainties are calculated for each PICS. Table 4.15 shows the resulting temporal uncertainty estimates of each PICS after performing the trending using the BRDF PNP technique. As with the initial normalization technique, the overall uncertainties are well within 2%, with the exception of the Coastal/Aerosol and Blue bands for the Libya-1 and Niger-2 PICS, where the estimated uncertainties are on the order of 3%. For both techniques, the estimated uncertainty for the SWIR1 band is less than 1%.

Table 4.16 gives the results of a percentage difference comparison, for each band, between the derived BRDF PNP TOA for each PICS and the Libya-4 BRDF optimal mean value. For all 7 bands and for all PICS, the differences are within ± 1%.

PICS_BRDF PNP Uncertainty	C/A	Blue	Green	Red	NIR	SWIR1	SWIR2
Libya-4	1.17%	1.34%	1.31%	1.16%	0.81%	0.57%	1.84%
Libya-1	3.04%	2.95%	1.51%	1.02%	0.68%	0.70%	1.53%
Niger-1	1.17%	1.20%	0.94%	0.86%	0.66%	0.78%	1.53%
Niger-2	3.04%	3.11%	1.57%	1.26%	1.06%	0.48%	2.07%
Sudan-1	1.53%	1.43%	0.89%	1.08%	0.71%	0.60%	1.89%
Egypt-1	1.57%	1.69%	1.75%	1.74%	1.26%	0.75%	2.35%

Table 4.15 Percentage uncertainties of selected PICS after BRDF PNP trending.

%Mean diff	C/A	Blue	Green	Red	NIR	SWIR1	SWIR2
Libya-4	0.45%	0.48%	0.45%	0.40%	0.22%	0.14%	0.72%
Egypt-1	0.13%	0.25%	0.47%	0.55%	0.40%	0.14%	0.44%
Sudan-1	-0.05%	0.03%	0.24%	0.13%	0.01%	0.07%	0.28%
Niger-1	0.42%	0.39%	0.15%	0.18%	0.28%	0.40%	0.40%
Niger-2	0.18%	0.19%	0.16%	0.06%	0.16%	0.00%	-0.35%
Libya-1	0.58%	0.53%	0.16%	0.02%	0.15%	0.40%	0.25%

Table 4.16 % difference for BRDF PNP TOA reflectance vs BRDF Optimal mean of Libya-4 for 6 PICS.

Figure 4.14 shows the BRDF corrected Super PICS trends for the VNIR and SWIR1 bands. Between approximately DSL 250 and DSL 1050, the trends appear to be relatively flat with little variation. Greater variability can be observed in the DSL 50 to DSL 250 period (early 2013), most noticeably in the Red and NIR bands. Greater variability is also apparent in the 2016 data (approximately DSL 1250 onwards), again more noticeably in the Red and NIR bands.

Figure 4.15 shows the BRDF corrected Super PICS trends for the Coastal/Aerosol and SWIR2 bands. For the Coastal/Aerosol band, the trend appears to be relatively flat with little variation. Greater variability is apparent in early 2013 and throughout 2016 in the Coastal/Aerosol band, and quite noticeable in the SWIR2 band. The results suggest that additional corrections for seasonal variability will be needed to reduce SWIR2 band uncertainty.

Based on the refined PNP technique, Super PICS trending analysis and drift estimates indicate that the drift is generally within 0.2% per year across all spectral bands.

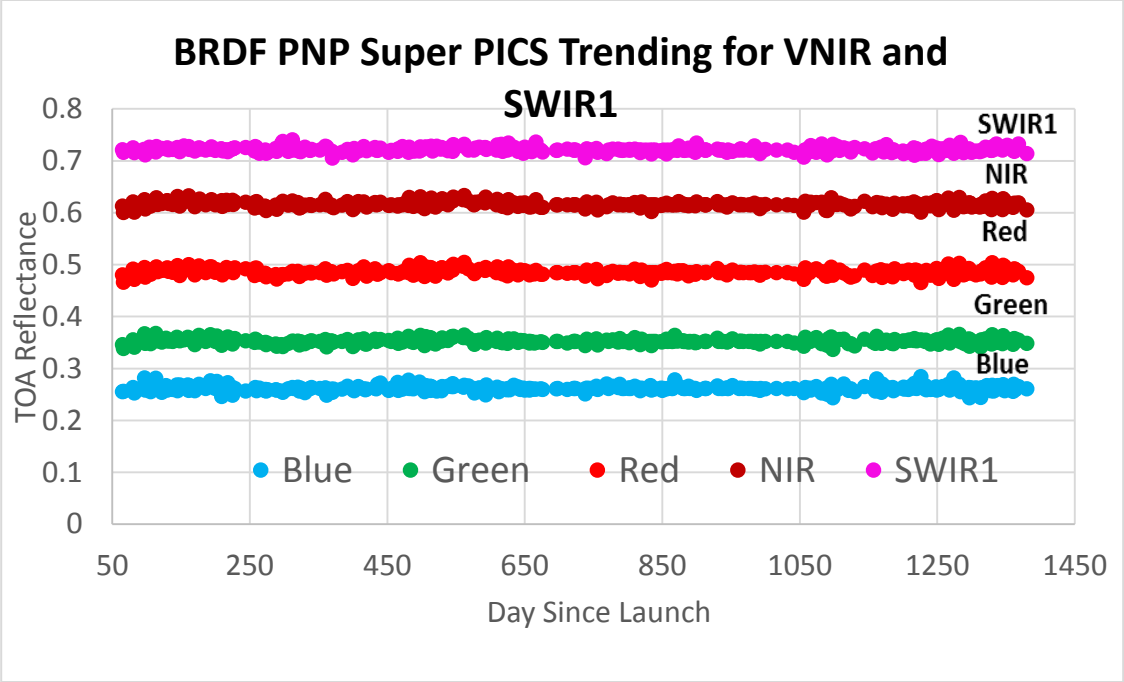

Figure 4.14. BRDF PNP Super PICS trending for 6 PICS (VNIR and SWIR1 bands).

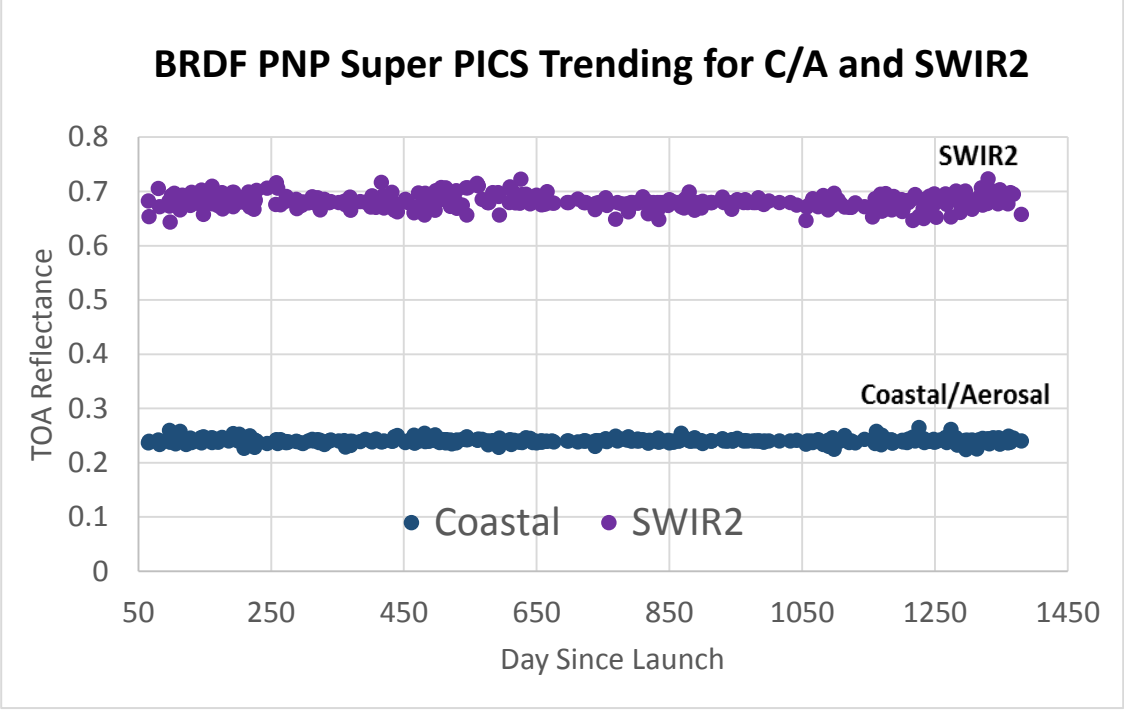

Figure 4.15. BRDF PNP Super PICS trending for 6 PICS for C/A and SWIR2 bands.

The same statistical analysis performed for the initial PNP Super PICS dataset was performed for the BRDF corrected Super PICS dataset. The results of this analysis are given in Table 4.17, and in general appear to be consistent with the results from the previous analysis. For the Coastal/Aerosol, Blue, Green and SWIR1 bands the estimated drifts are less than 0.1% per year. For the Red, NIR and SWIR2 the estimated drift is on the order of 0.15% to 0.2% per year. For all spectral bands, the corresponding temporal uncertainties for the Super PICS dataset are on the order of 2%. For all spectral bands except NIR, the p-values are significantly higher for the BRDF corrected Super PICS dataset than for the initial PNP Super PICS dataset. The differences are most significant in the Coastal/Aerosol and Blue bands, where the p-values increase from approximately (0.07, 0.15) for the initial dataset to approximately (0.38, 0.53) for the BRDF corrected dataset. Significant increases can also be seen in the SWIR1 and SWIR2 bands, where the p-values increase from approximately (0.005, 0.0004) for the initial dataset to approximately (0.08, 0.1) for the BRDF corrected dataset. These differences suggest that removal of BRDF effects provide better results of slope test for all spectral bands.

BRDF-PNP Super PICS	C/A	Blue	Green	Red	NIR	SWIR1	SWIR2
%Drift/year	-0.09	-0.07	-0.09	-0.13	-0.14	-0.06	-0.17
2Sigma	0.21	0.22	0.14	0.13	0.09	0.07	0.20
p-value Slope = 0	0.3765	0.5330	0.2273	0.0454	0.0021	0.0794	0.0964
Uncertainty	2.05%	2.07%	1.38%	1.26%	0.91%	0.66%	1.93%

Table 4.17 BRDF PNP Super PICS statistical analysis for the estimation of drift for OLI.

4.2.3 BRDF corrected PNP Drift Estimates for OLI:

Gain drift in percentage per year is estimated from trending of individual BRDF PNP PICS data, the weighted average of the BRDF PNP PICS data and the combined BRDF Super PICS data. Table 4.18 gives the estimates for all BRDF PNP PICS along with the estimates for the weighted average and BRDF Super PICS dataset, Table 4.19 shows the corresponding 2-sigma uncertainties.

Percentage drift per year for BRDF PNP analysis								
BRDF PNP Drift	**Libya-4**	**Libya-1**	**Niger-1**	**Niger-2**	**Sudan-1**	**Egypt-1**	**W.avg**	**BRDF Super PICS**
C/A	-0.46	0.70	-0.12	-0.54	-0.26	0.19	-0.21	-0.09
Blue	-0.56	0.66	-0.05	-0.53	-0.16	0.32	-0.17	-0.07
Green	-0.46	0.09	0.09	-0.47	-0.08	0.37	-0.10	-0.09
Red	-0.37	-0.20	0.09	-0.49	-0.07	0.30	-0.16	-0.13
NIR	-0.33	-0.13	-0.01	-0.43	-0.05	0.11	-0.15	-0.15
SWIR1	-0.14	-0.08	-0.01	-0.14	0.01	-0.02	-0.09	-0.06
SWIR2	-0.36	-0.29	0.13	-0.42	-0.24	0.18	-0.19	-0.17

Table 4.18 Percentage drift per year for each PICS using BRDF PNP technique.

2 sigma values for BRDF PNP analysis								
BRDF PNP 2-sigma	**Libya-4**	**Libya-1**	**Niger-1**	**Niger-2**	**Sudan-1**	**Egypt-1**	**W.avg**	**BRDF Super PICS**
C/A	0.25	0.82	0.35	0.76	0.39	0.36	0.68	0.21
Blue	0.28	0.80	0.36	0.78	0.37	0.39	0.69	0.22
Green	0.29	0.41	0.29	0.38	0.23	0.40	0.46	0.14
Red	0.26	0.27	0.26	0.29	0.28	0.40	0.41	0.13
NIR	0.17	0.18	0.20	0.24	0.18	0.29	0.29	0.09
SWIR1	0.13	0.19	0.24	0.12	0.15	0.17	0.18	0.07
SWIR2	0.43	0.41	0.47	0.52	0.48	0.55	0.54	0.20

Table 4.19 2-Sigma values for each PICS using BRDF PNP technique.

BRDF correction of the original image data can reduce the scatter of data and greatly improve the result of trending analysis and drift estimation. The BRDF effect appears to

be band-dependent, as BRDF correction generally result in lower estimated drift in the longer wavelength bands. In the shorter wavelength bands, the effect may also be site-dependent. For the Libya-4 PICS, the result of drift estimates has decreased significantly for all spectral bands; in the Blue band, the estimated drift decreases from approximately -0.8% per year with the initial PNP technique to -0.55% per year with the BRDF corrected PNP technique. On the other hand, for the Libya-1, Niger-2 and Sudan-1 PICS, the estimated drifts in the Coastal/Aerosol and Blue bands have increased with the BRDF PNP technique. For the Coastal/Aerosol band in Libya-1, the estimated drift is approximately -0.13% per year with the initial PNP technique; with the BRDF corrected PNP technique it is approximately -0.70% per year.

Overall, the drift estimates for the BRDF Super PICS dataset have decreased for all spectral bands, from within -0.3% per year to within -0.2% per year. A similar decrease can also be seen for the BRDF corrected weighted average method, from within -0.35% to -0.25% per year for all spectral bands. Finally, the drift estimates for the BRDF corrected PNP technique with super PICS dataset in all spectral bands tend to be lower than the corresponding BRDF corrected weighted average estimates. Figure 4.16 shows the combined plot of these estimates.

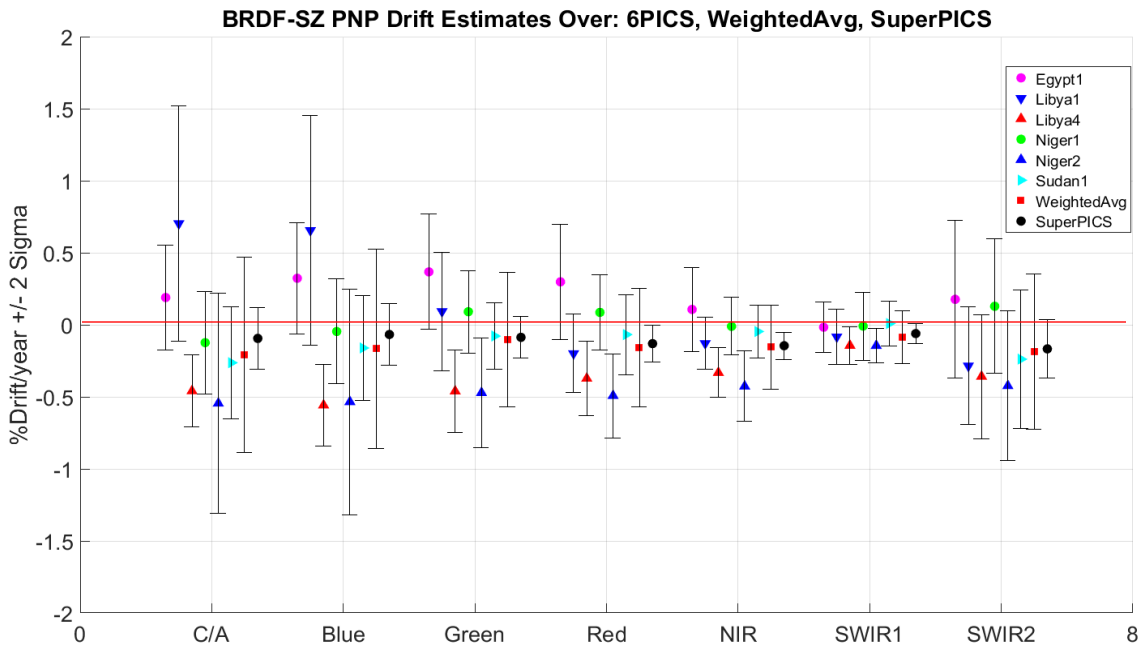

Figure 4.16. % Drift comparison for BRDF PNP from each PICS, weighted avg. & Super PICS.

4.3 BRDF corrected PNP Uncertainty Analysis:

Worst-case bin Analysis:

This Section shows the effect of the number of histogram bins on the resulting optimal region for each PICS, as derived according to the "worst-case number of bins" uncertainty analysis described in Section 3.3.2. The analysis is performed using the BRDF corrected image data. Recall that equations (6a) – (9) from Section 3.1.2 are used to generate the optimal regions. For all PICS, 10, 15, 20, and 30 are used as the selected number of bins when generating the histograms.

The summary results for each PICS are presented as follows:

1. Figures showing the optimal region resulting from histograms with a given number of bins.

2. Tables showing the mean TOA reflectance in the ROI selected from the optimal region. Values in blue indicate the ROI optimal value used to derive the trending results presented in this chapter. Values in green indicate the mean TOA reflectance derived from the "worst-case number of bins" analysis.
3. Figures showing the percentage difference between the ROI TOA reflectance mean used for trending purposes, and the TOA reflectance calculated from the stable region given a specific number of histogram bins.
4. A given number of histogram bins is considered the "worst-case" estimate if the percentage difference in ROI mean TOA reflectance and stable region mean TOA reflectance is greatest in at least 2 bands.

4.3.1 Libya-1:

Figures 4.17 (a) – (d) show the optimal area mask generated for the Libya-1 PICS. The region generated from the 10 and 30 bin histogram analyses has a prominent "tail" at the southeast corner; with a histogram using 10 bins, the resulting tail extends to the southern border of the site. The tail is much less pronounced in the regions derived from the 15 and 20 bins histogram analyses. The region generated from the 20 bins analysis appears to be most consistent with the region shown in Figure 4.1, which was generated using the initial PNP technique.

Libya-1	C/A	Blue	Green	Red	NIR	SWIR1	SWIR2
BRDF ROI	0.1997	0.2106	0.3059	0.4899	0.6338	0.7541	0.6293
Bin10	0.2013	0.2122	0.3053	0.4914	0.6376	0.7589	0.6308
Bin15	0.2013	0.2124	0.3057	0.4924	0.639	0.7604	0.6319
Bin20	0.2014	0.2124	0.3056	0.4925	0.6393	0.7606	0.6317
Bin30	0.2013	0.2124	0.3056	0.4924	0.6392	0.7606	0.6318

Table 4.20 BRDF OAM mean values for (different bins & selected ROI) Libya-1.

Table 4.20 gives the optimal mean TOA reflectance for the selected Libya-1 ROI, as derived from equations (10) – (12). Overall, the difference between the ROI optimal mean TOA reflectance and the TOA reflectance estimates from the "worst- number of bins" analysis for Libya-1 are less than 1% for all selected number of bins. These differences are shown in Figure 4.18. The Green and SWIR2 bands show the smallest differences, suggesting that for this PICS, the Green and SWIR2 bands are relatively insensitive to changes in the number of histogram bins.

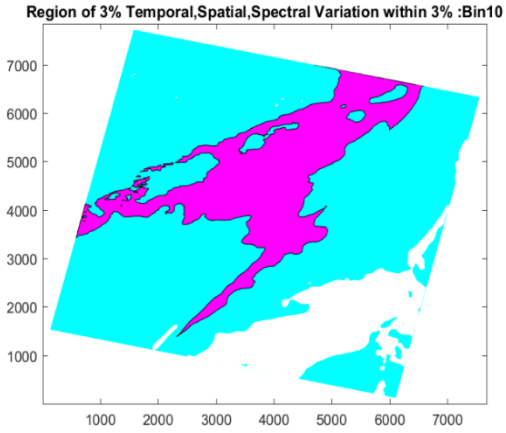

a) Histogram of 10 bins

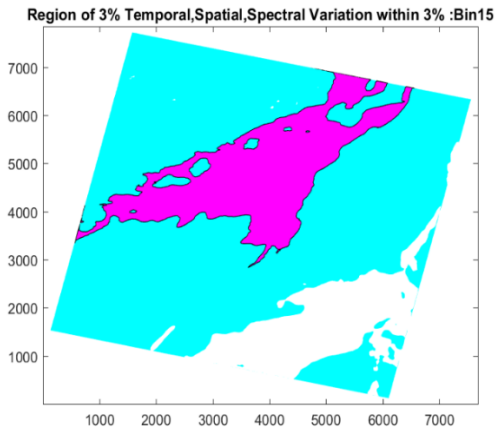

b)Histogram of 15 bins

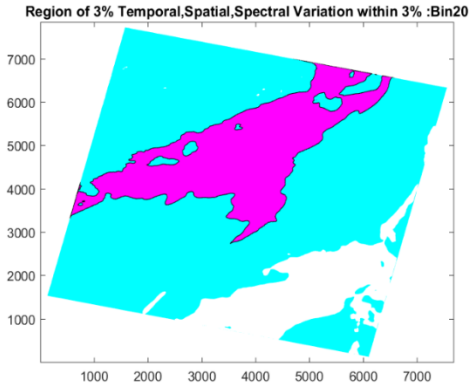

c) Histogram of 20 bins

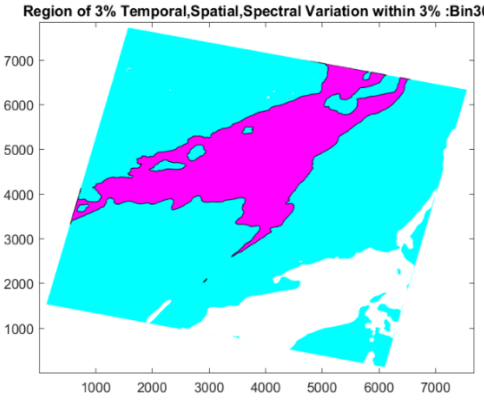

d) Histogram of 30 bins

Figure 4.17. OAM within the Libya-1 PICS for different number of histogram bins.

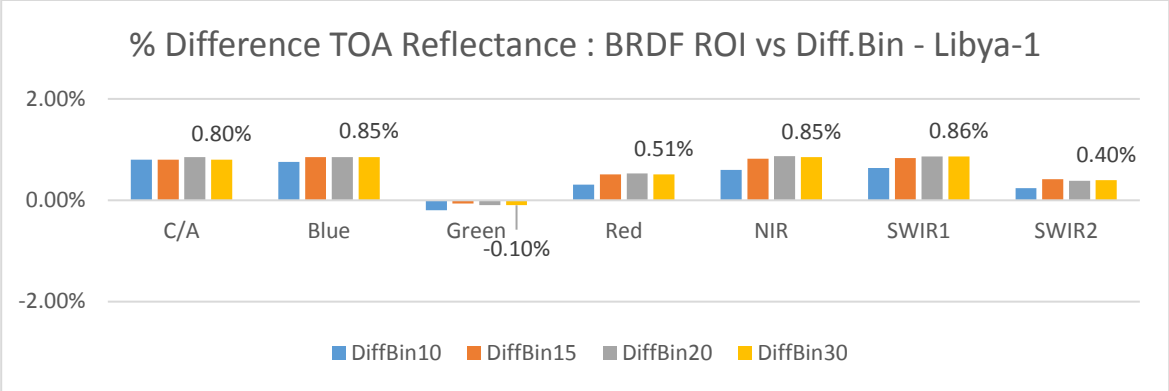

Figure 4.18. "Worst-case bin analysis" (sensitivity test) for Libya-1 site.

4.3.2 Sudan-1:

Figures 4.19 (a) – (d) show the optimal area mask generated for the Sudan-1 PICS. Overall, the BRDF corrected OAM regions are similar; some differences can be seen due to the varying number of histogram bins used in the analysis. Each of the BRDF corrected regions cover more area than the region shown in Figure 4.2 that was generated with the initial PNP technique. This can be most clearly observed with the northern area of the region. In Figure 4.2, only a slight tail in the western portion is present. In all of the regions derived from BRDF corrected data, the western part of that area has almost completely filled in. The optimal mean BRDF TOA reflectance values for corresponding regions were shown in Table 4.21.

Figure 4.20 shows the difference between the optimal mean TOA reflectance value for the selected ROI and the TOA reflectances derived from the ""worst-case number of bins" analysis. As might be expected, the greater sensitivity to changes in the optimal region boundaries corresponds to greater variability in the resulting optimal mean TOA reflectances, on the order of 1.05% for all 7 bands. For this PICS, the Green, Red, and SWIR1 bands appear to be more sensitive to changes in the number of histogram bins.

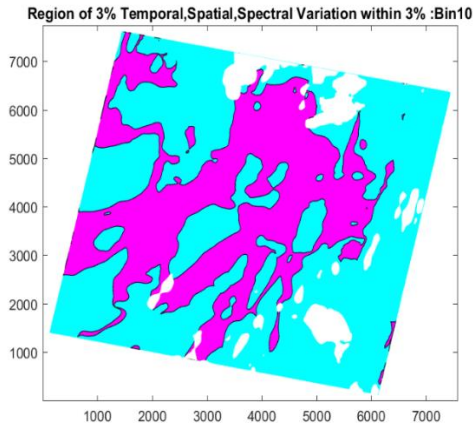

a) Histogram of 10 bins

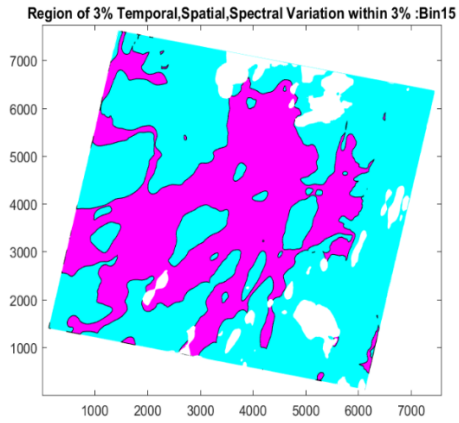

b)Histogram of 15 bins

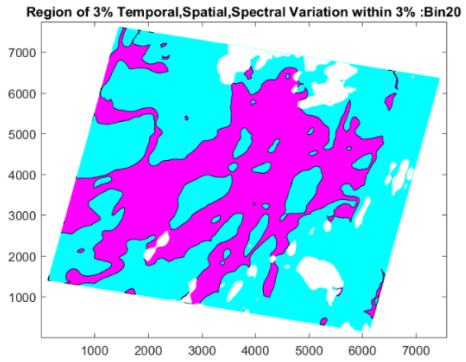

c) Histogram of 20 bins

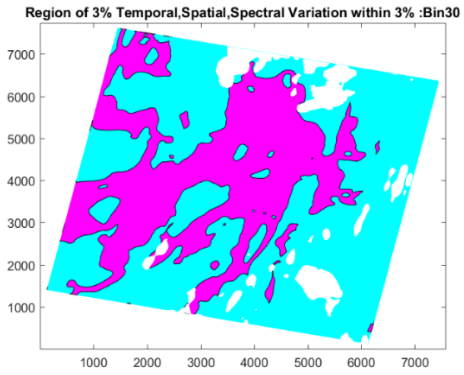

d) Histogram of 30 bins

Figure 4.19. OAM within the Sudan-1 PICS for different number of histogram bins.

Sudan-1	C/A	Blue	Green	Red	NIR	SWIR1	SWIR2
BRDF ROI	0.2175	0.2293	0.3181	0.4669	0.5820	0.7245	0.6738
Bin10	0.2177	0.2307	0.3215	0.4731	0.5845	0.7166	0.6703
Bin15	0.2169	0.2298	0.3209	0.4734	0.585	0.7183	0.6718
Bin20	0.2171	0.2301	0.3213	0.4735	0.585	0.7173	0.6713
Bin30	0.2176	0.2304	0.3206	0.4713	0.5828	0.7169	0.6703

Table 4.21 BRDF OAM mean values for (different bins & selected ROI) Sudan-1.

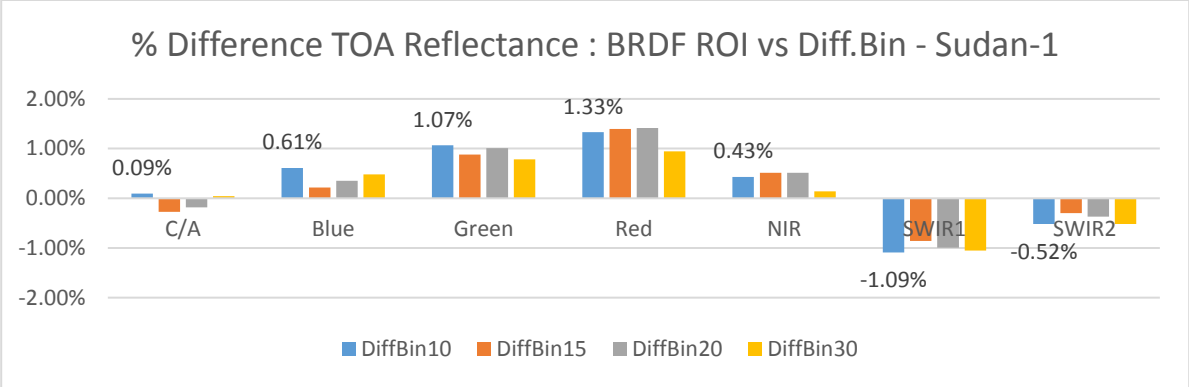

Figure 4.20. "Worst-case bin analysis" (sensitivity test) for Sudan-1 site.

4.3.3 Niger-1:

Figures 4.21 (a) – (d) show the optimal area mask generated for the Niger-1 PICS. In general, the region is confined to the center part of the site. Among the BRDF corrected regions, the region generated from the 10 bin analysis is clearly the smallest area, and is smaller in area than the region shown in Figure 4.3 generated with the initial PNP technique. This can be seen in the gap at the center of the region. With 10 histogram bins, the gap almost cuts the region into two parts; with more than 10 bins, the gap only extends to the center of the region. Table 4.22 shows the coresponding optimal mean TOA reflectance values.

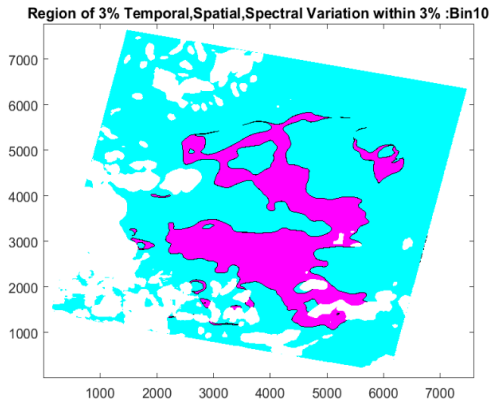

a) Histogram of 10 bins

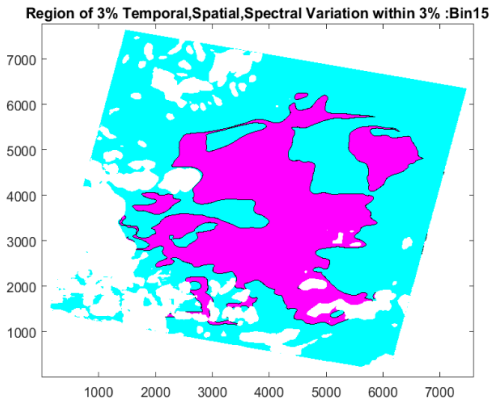

b)Histogram of 15 bins

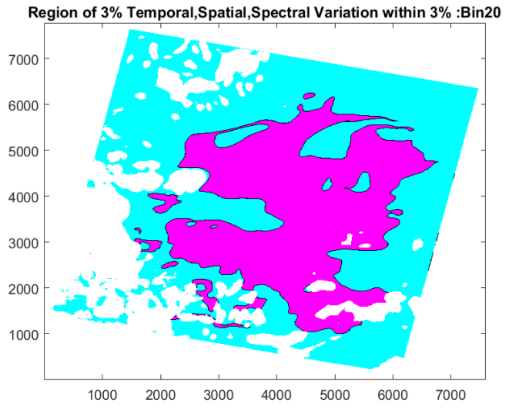

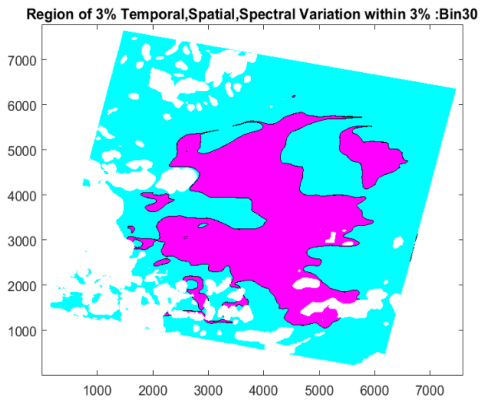

c) Histogram of 20 bins d) Histogram of 30 bins

Figure 4.21. OAM within the Niger-1 PICS for different number of histogram bins.

Niger-1	C/A	Blue	Green	Red	NIR	SWIR1	SWIR2
BRDF ROI	0.2334	0.2455	0.3262	0.4720	0.5967	0.7312	0.6526
Bin10	0.2346	0.2468	0.3289	0.4727	0.5982	0.7323	0.6521
Bin15	0.2332	0.2451	0.3265	0.4708	0.5964	0.7314	0.6513
Bin20	0.2345	0.2466	0.3284	0.4724	0.5981	0.7324	0.6522
Bin30	0.2336	0.2456	0.3276	0.4723	0.5981	0.7325	0.6524

Table 4.22 BRDF OAM mean values for (different bins & selected ROI) Niger-1.

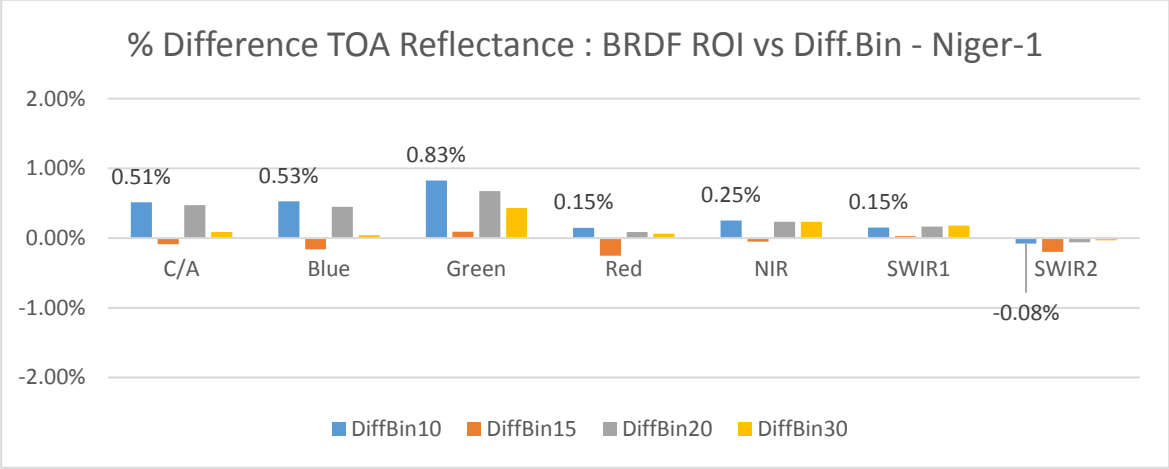

Figure 4.22. "Worst-case bin analysis" (sensitivity test) for Niger-1 site.

Figure 4.22 shows the difference between the optimal mean TOA reflectance value for the selected ROI and the TOA reflectances derived from the "worst-case bin number of bins" analysis. The differences for this PICS are greater in the shorter wavelength bands. However, none of the differences exceed 1%. The smallest differences are found in the longer wavelength bands, where the differences for all selected number of bins are less than 0.3%.

4.3.4 Egypt-1:

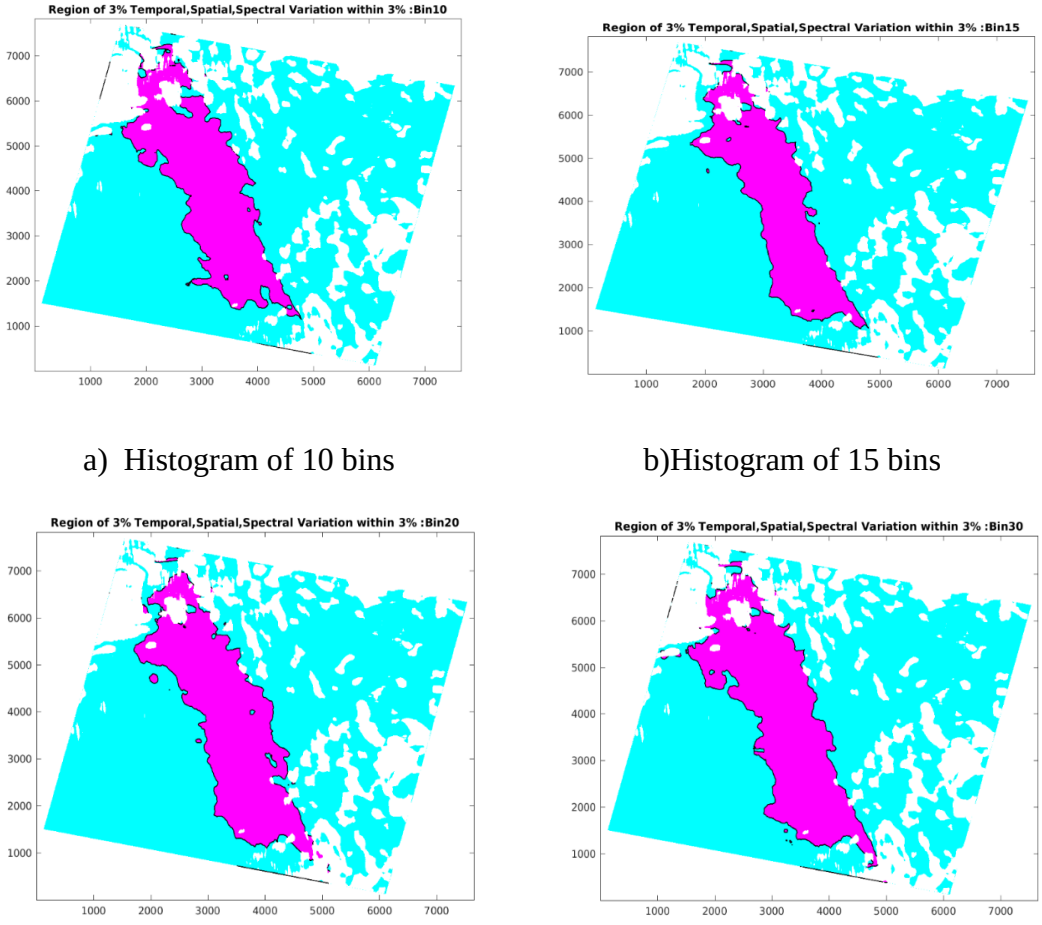

a) Histogram of 10 bins

b)Histogram of 15 bins

c) Histogram of 20 bins

d) Histogram of 30 bins

Figure 4.23. OAM within the Egypt-1 PICS for different number of histogram bins.

Figures 4.23 (a) – (d) show the optimal area mask generated for the Egypt-1 PICS. Among the BRDF regions generated from BRDF corrected data, the boundary is consistent with respect to the number of histogram bins used in the analysis. When compared to the region generated using the initial PNP technique (shown in Figure 4.4), there is a significant difference; the region generated from the BRDF corrected data extends much further to the northwest. The Table 4.23 shows the coresponding optimal mean TOA reflectance values. Figure 4.24 shows the difference between the optimal mean TOA reflectance value for the selected ROI and the TOA reflectances derived from the "worst-case number of bins" analysis. The estimated TOA reflectances are consistently smaller than the ROI optimal mean TOA for all 7 bands, across all selected number of histogram bins. Overall, the differences are on the order of 1

Egypt-1	C/A	Blue	Green	Red	NIR	SWIR1	SWIR2
BRDF ROI	0.2312	0.2449	0.3299	0.4633	0.5979	0.7273	0.6482
Bin10	0.2306	0.2440	0.3272	0.4592	0.5939	0.7222	0.6448
Bin15	0.2293	0.2427	0.3268	0.4596	0.5945	0.7227	0.6435
Bin20	0.2287	0.242	0.3263	0.4593	0.594	0.7228	0.6433
Bin30	0.2307	0.2442	0.3274	0.4595	0.5941	0.7223	0.6447

Table 4.23 BRDF OAM values for (different bins & selected ROI) Egypt-1.

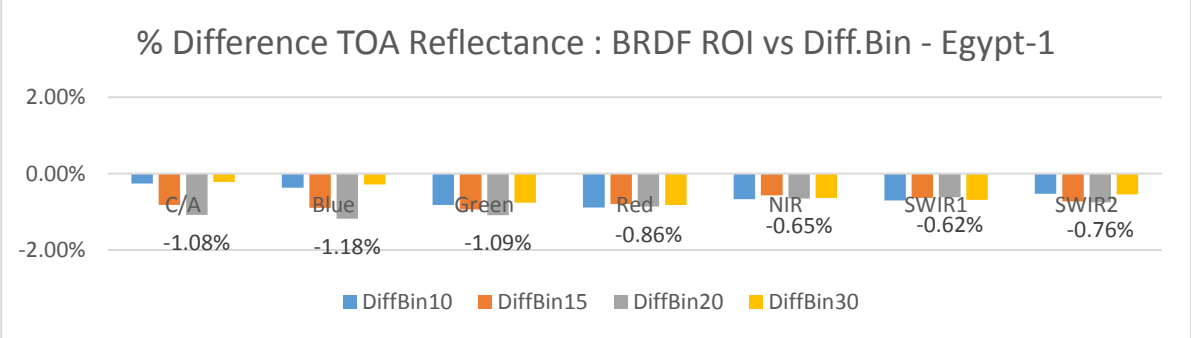

Figure 4.24. "Worst-case bin analysis" (sensitivity test) for Egypt-1 site.

4.3.5 Niger-2:

Figures 4.25 (a) – (d) show the optimal area mask generated for the Niger-2 PICS. Among the BRDF corrected data, the region generated using 10 histogram bins is the smallest in area. The southernmost part appears to fill in when using 15 and 20 bins, and thins out again when 30 bins are used. Interestingly, the region generated with the initial PNP technique is generally larger in area, and appears to be most consistent with the region generated with a histogram of 20 bins. Table 4.24 shows the coresponding optimal mean TOA reflectance values.

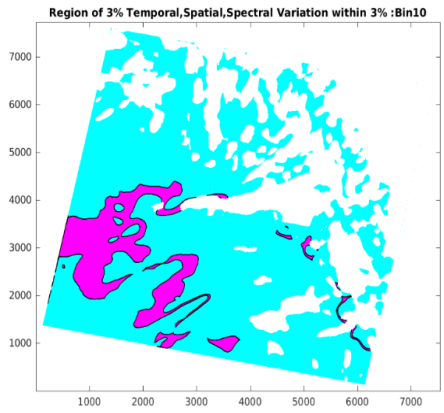

a) Histogram of 10 bins

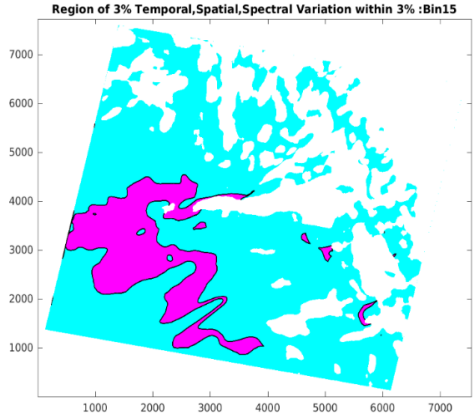

b)Histogram of 15 bins

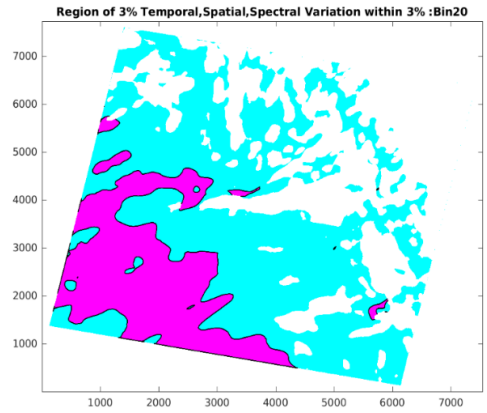

c) Histogram of 20 bins

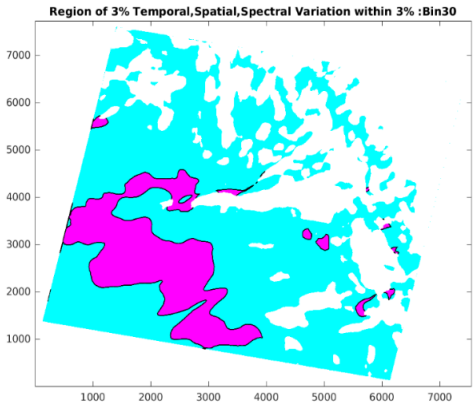

d) Histogram of 30 bins

Figure 4.25. OAM within the Niger-2 PICS for different number of histogram bins.

Figure 4.26 shows the difference between the optimal mean TOA reflectance value for the selected ROI and the TOA reflectances derived from the "worst-case number of bins" analysis. The difference values estimated for this PICS suggest marked sensitivity to changes in the number of histogram bins that is somewhat inconsistent both within a band and across bands.

Niger-2	C/A	Blue	Green	Red	NIR	SWIR1	SWIR2
BRDF ROI	0.2233	0.2320	0.2978	0.4120	0.5151	0.6628	0.5941
Bin10	0.2207	0.23	0.297	0.4152	0.5165	0.6626	0.5899
Bin15	0.2214	0.2306	0.2971	0.4142	0.5156	0.6615	0.589
Bin20	0.2232	0.2327	0.3007	0.4176	0.5204	0.6682	0.5965
Bin30	0.2220	0.2315	0.2982	0.4150	0.5161	0.6605	0.5878

Table 4.24 BRDF OAM mean values for (different bins & selected ROI) Niger-2.

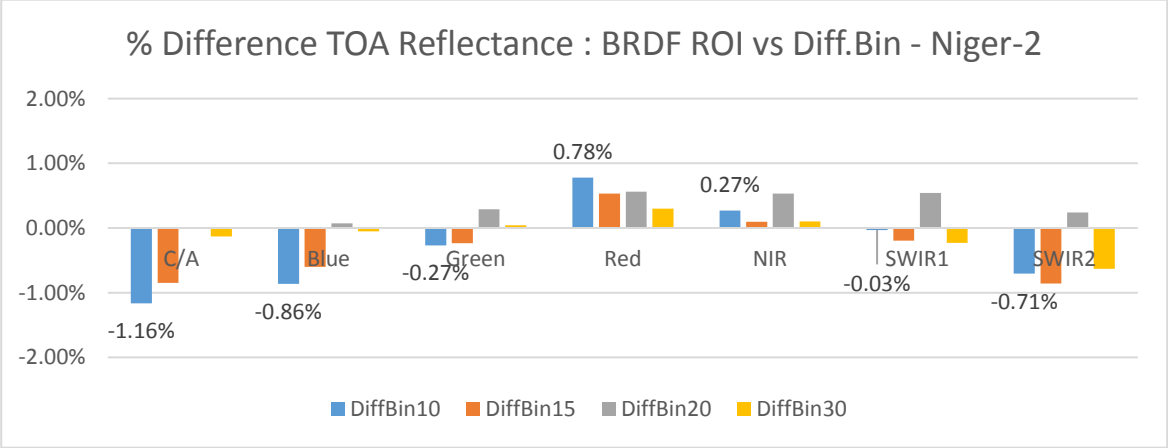

Figure 4.26. "Worst-case bin analysis" (sensitivity test) for Niger-2 site.

4.3.6 Libya-4:

Figures 4.27 (a) – (d) show the optimal area mask generated for the Libya-4 PICS. The optimal region boundaries appear to be quite consistent as the histogram number of bins

increased beyond 10. It is not currently known whether this consistency would remain if the number of bins is increased beyond 30. For this PICS at least, it is possible that there is a large "sweet-spot" in the number of bins that can be used when generating the histogram. The region generated with any number of histogram bins is also generally consistent with what was generated using the initial PNP technique. The Table 4.25 shows the coresponding optimal mean TOA reflectance values.

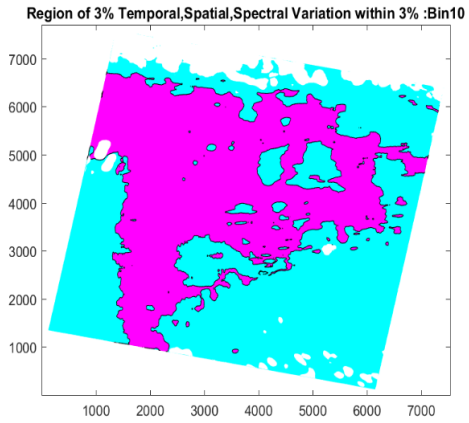

a) Histogram of 10 bins

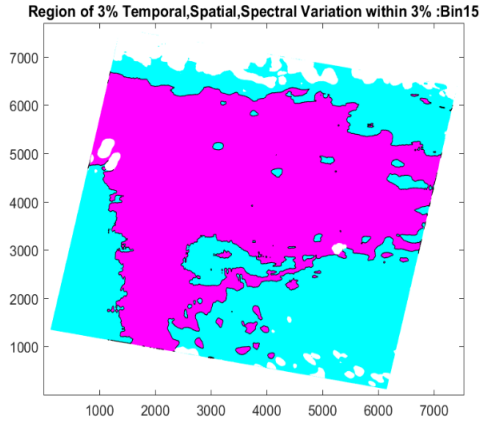

b) Histogram of 15 bins

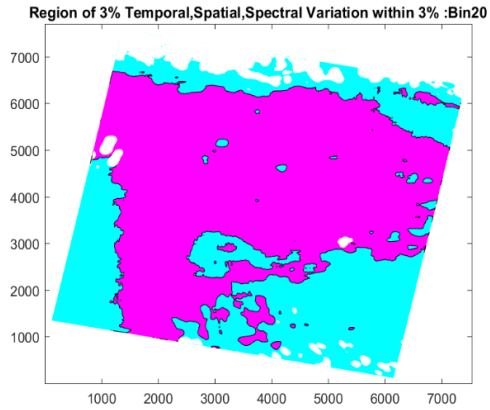

c) Histogram of 20 bins

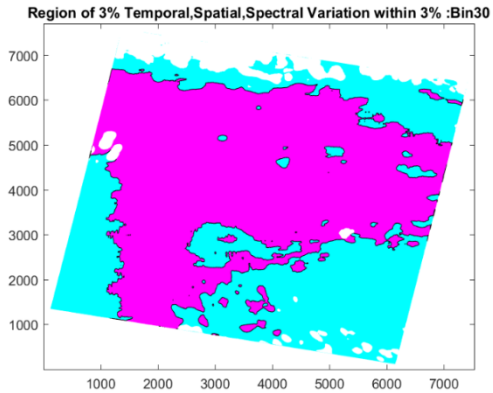

d) Histogram of 30 bins

Figure 4.27. OAM within the Libya-4 PICS for different number of histogram bins.

Libya-4	C/A	Blue	Green	Red	NIR	SWIR1	SWIR2
BRDF ROI	0.2399	0.2613	0.3521	0.4850	0.6154	0.7205	0.6795
Bin10	0.2409	0.2609	0.3488	0.4784	0.6113	0.7178	0.6709
Bin15	0.2408	0.2606	0.3484	0.478	0.6105	0.7178	0.6717
Bin20	0.2406	0.2605	0.3487	0.4784	0.6108	0.7180	0.6714
Bin30	0.2407	0.2605	0.3485	0.4782	0.6107	0.7179	0.6714

Table 4.25 BRDF OAM values for (different bins & selected ROI) Libya-4.

Figure 4.28 shows the difference between the optimal mean TOA reflectance value for the selected ROI and the TOA reflectances derived from the "worst-case number of bins" analysis. Surprisingly, differences ranging from 1% to 1.5% are observed in the Green, Red, and SWIR2 bands. For all 7 bands but the Coastal/Aerosol, the ROI optimal mean TOA reflectances are less than the estimated mean TOA reflectances.

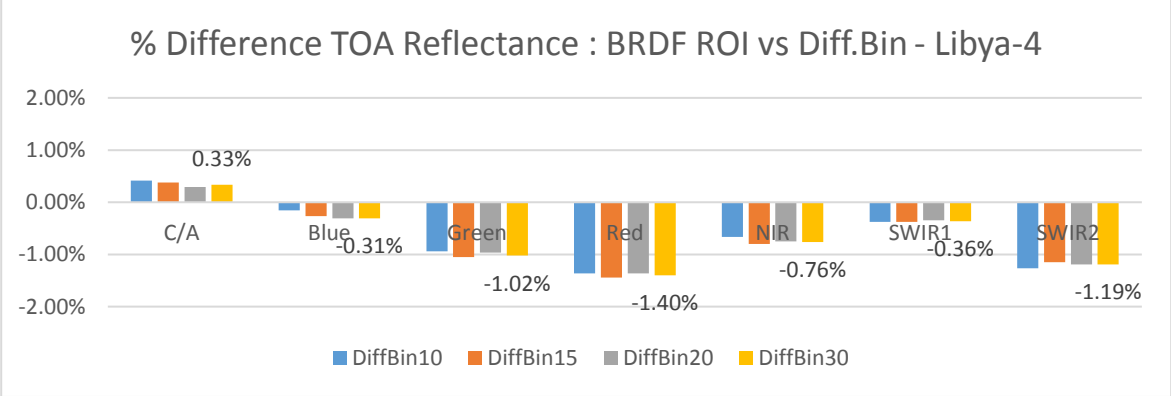

Figure 4.28. "Worst-case bin analysis" (sensitivity test) for Libya-4 site.

Table 4.26 shows the uncertainties of the "worst-case bin analysis" for each PICS. Among all the PICS, the Egypt-1 results seem to be the most sensitive to the selected number of histogram bins in most spectral bands. Overall, the differences were within 1.5% for all PICS. The largest difference, 1.4%, is observed for the Red band in Libya-4; the smallest

difference, 0.03%, is observed for the SWIR1 band of Niger-2. These results suggest that the number of bins to use when generating the histogram may be site-dependent.

"worst-case bin" Uncertainty	No. bins	C/A	Blue	Green	Red	NIR	SWIR1	SWIR2
Libya-4	30	0.33%	0.31%	1.02%	1.40%	0.76%	0.36%	1.19%
Egypt-1	20	1.08%	1.18%	1.09%	0.86%	0.65%	0.62%	0.76%
Libya-1	30	0.80%	0.85%	0.10%	0.51%	0.85%	0.86%	0.40%
Niger-1	10	0.51%	0.53%	0.83%	0.15%	0.25%	0.15%	0.08%
Niger-2	10	1.16%	0.86%	0.27%	0.78%	0.27%	0.03%	0.71%
Sudan-1	10	0.09%	0.61%	1.07%	1.33%	0.43%	1.09%	0.52%

Table 4.26 "Worst-case bin analysis" Uncertainty of each PICS after BRDF PNP.

4.4 Estimation of Final Uncertainty for BRDF corrected PNP:

Table 4.27 shows the sources of uncertainty (units of TOA reflectance) determined for this technique and presents the final uncertainty estimate as determined from equation (24). Equation (23) was used to estimate the inherent temporal uncertainty for each band across all PICS. The uncertainty from the "worst-case bin analysis" is also determined as a spatial uncertainty which may still inhibit in the process. The final uncertainty of the BRDF PNP technique is estimated as better than 2% for all bands except C/A, Blue and SWIR2 bands. The estimated uncertainties are greater in the Coastal/Aerosol, Blue, and SWIR2 bands, which are within 3%.

As mentioned before, all of the analysis results presented in this thesis are generated from Landsat-8 OLI image data, which has an estimated inherent uncertainty in all bands of

less than 3% with respect to spectral TOA reflectance [17]. For the datasets used in this analysis, the estimated final uncertainty is within the accepted spectral reflectance uncertainty for the OLI sensor.

Uncertainty	CA	Blue	Green	Red	NIR	SWIR1	SWIR2
BRDF Super PICS	2.05%	2.07%	1.38%	1.26%	0.91%	0.66%	1.93%
Bin Analysis (spatial)	0.66%	0.72%	0.73%	0.84%	0.54%	0.52%	0.61%
Temporal Uncertainty across PICS	1.65%	1.65%	1.13%	0.95%	0.69%	0.54%	1.81%
Final	2.71%	2.74%	1.93%	1.79%	1.26%	1.00%	2.72%

Table 4.27 Estimation of final uncertainty for BRDF PNP technique.

As mention earlier, the preceding analysis was performed using the OLI sensor. The results from this analysis can also be used for any other sensors by applying appropriate spectral band adjustment factor corrections. As an example, a commercial satellite, Planet Labs, is using the initial PNP technique. The results of this process will form a time series referenced back to Libya-4 that can be used to trend the gain of an instrument over time. These time series can also can be used for cross-calibration between sensors.

Implementation of the calibration procedure developed for this project with the Planet Labs fleet represents a major step forward in cross-calibration of optical remote sensing satellites. Heretofore, cross-calibration has implicitly meant application to only a handful of satellites at a time—six or less. Cross-calibration of the Planet Labs flock of dozens of satellites is unprecedented and will provide an excellent opportunity to observe the merits and limitations of this approach.

CHAPTER 5

CONCLUSION

5.1 Summary:

A new technique is presented that combines sensor observations of multiple PICS into a single time series dataset with greater temporal resolution. The technique was applied to six Saharan PICS locations selected for their temporal and spatial uniformity. OLI image data from five of these sites were normalized to data from the Libya-4 PICS reference. The temporal resolution (OLI revisit time) resulting from application of this technique increased by approximately a factor of three to four i.e. acquiring an image for every 3 to 4 days. Adding correction of BRDF effects using a quadratic function of solar zenith angle and TOA reflectance, a calibration result consistent with current onboard and vicarious calibration results was achieved. With this technique, other sensors can potentially detect early signs of response changes through cross calibration with OLI (well-calibrated sensor [17]). In addition, this technique demonstrates why Libya-4 is considered a suitable reference PICS, not only due to its spatial and temporal stability, but also due to its largest 3% temporal, spatial and spectral region.

Using the initial PNP technique, the estimated drift for the Super PICS dataset was on the order of -0.25% per year for the VNIR and SWIR1 bands and -0.4% per year for the SWIR2 band. Using the BRDF corrected PNP technique, the estimated drifts were on the order of -0.15% per year. BRDF correction reduced the estimated drifts by approximately 50%. These reduced drift estimates agree well with the on-board calibrator estimates shown in [24]. The corresponding Super PICS uncertainties for both methods were on the

order of 2% for all solar reflective bands. For most bands, the PNP weighted average drift estimates were normally larger at shorter wavelengths and at longer wavelengths they tend to be same as PNP Super PICS estimates. The weighted average drift estimates were, surprisingly, worse in all bands when using the BRDF corrected PNP technique. Based on the results of this analysis, it appears that calibration drift is better estimated using the combined BRDF Super PICS dataset rather than the BRDF weighted average of all data.

However, the results of the uncertainty analysis described in this chapter might not include the uncertainty of the sensor itself. Correlation may occur between the target and sensor which was not included in this thesis. If there is a correlation then, it will need to be included in equation (24).

5.2 Directions for Future work:

With the PNP and Refined PNP techniques described in this thesis, BaseMaps were calculated using 12 months of image data from 2015 for all 7 solar reflective bands. The resulting super PICS trend exhibits the least variability during that particular period, as shown in Figure 5.1 for the Green band (DSL 750 to DSL 1050). The variability in other years appears to be amplified. One potential enhancement to this technique is to derive the BaseMaps using the lifetime archive of cloud-free image data.

For the Refined PNP technique, the BRDF correction models include a linear term. The analysis described in Section 3.2.1 suggests the linear term may contribute little if anything to the overall BRDF response. The technique could be rerun with BRDF correction models generated with only the quadratic and constant terms, and compared to the new results with the current technique.

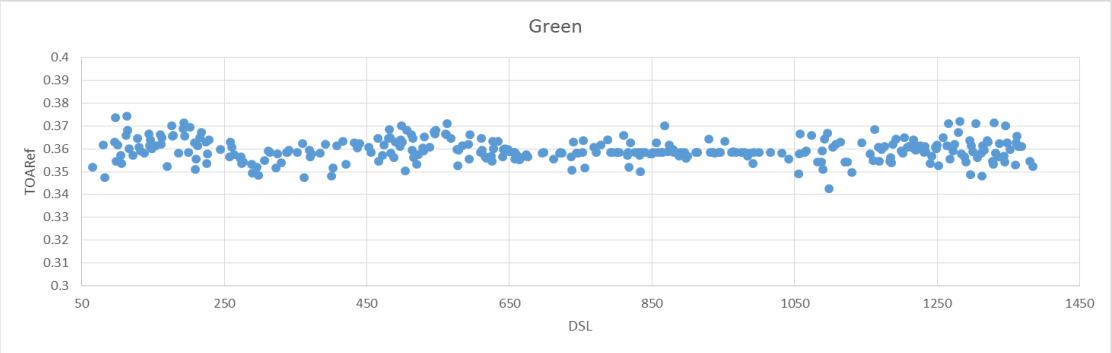

Figure 5.1. Zoom view of BRDF Super PICS results for Green band.

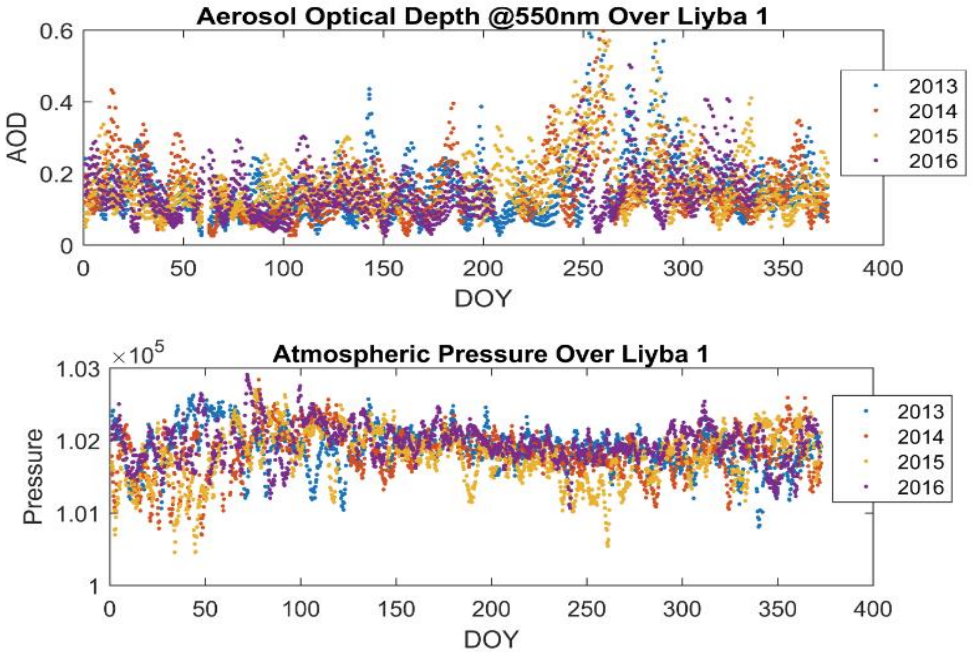

Figure 5.2. Aerosol optical depth and Atmospheric pressure over Libya-1 PICS.

The Super PICS trend data in Figure 5.1 shows residual seasonal variation, particularly in 2013. This variation is even more pronounced in the SWIR2 band. The seasonal variation is impacted by water vapor coming from the Mediterranean Sea, as well as perhaps sand and other dryer aerosol components. The technique as currently implemented may average out some of this variation. A further enhancement would include explicit correction of atmospheric effects.

From Figures 4.12 and 4.13, it has been clearly observed that the aerosol effect on recent image data for Libya-1 PICS suggests that the correction should be needed. Figure 5.2 shows the aerosol and atmospheric pressure effects at Libya-1 PICS.

Even though Libya-4 is currently the reference PICS for most calibration analyses, it appears to be showing more drift than expected. The maximum drift for this site was estimated on the order of -0.8% per year using the initial PNP technique, as shown in Table A.1 in the Appendix; the maximum estimated drift using the BRDF corrected PNP technique was estimated on the order of -0.6% per year, as shown in Table A.2. Leigh and Tabassum [25] identified the most temporally stable locations in North Africa for each individual reflective OLI band (Coastal, Blue, Green, Red, NIR, SWIR1, SWIR2) using the first three years of image data. These locations, shown in Figure 5.3, may be found to exhibit less drift than Libya-4, suggesting they would be a better choice for a reference PICS; at the very least, they could be useful as additional PICS to further enhance temporal resolution. It might be possible to group these sites into "dark" PICS and "bright" PICS and run this technique on both sets. This analysis could further improve overall calibration accuracy, as more of a sensor's dynamic range would be considered.

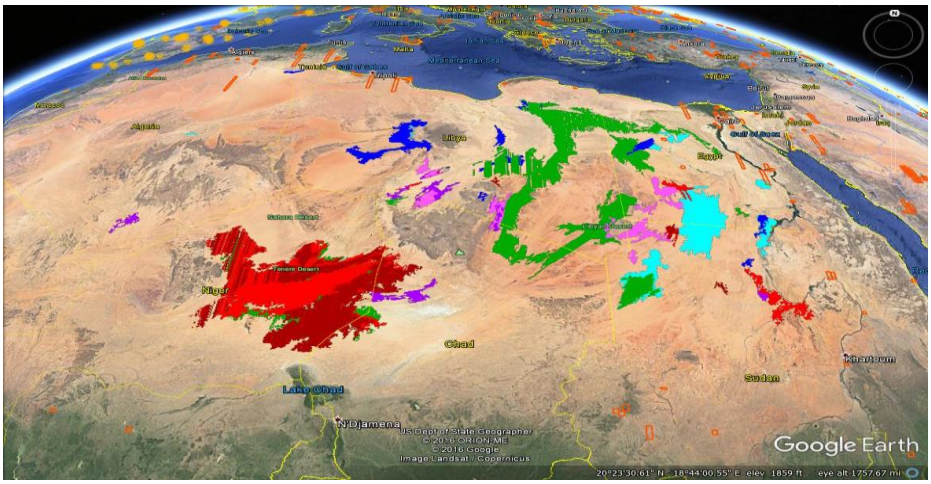

Figure 5.3. Most stable regions in North Africa for all 7 spectral bands [25].

REFERENCES

[1] D. Helder, B. Basnet, and D. Morstad, “Optimized identification of worldwide radiometric pseudo invariant calibration sites”, *Can. J. Remote Sens.*, vol. 36, no. 5, pp. 527-539, 2010. doi: 10.5589/m10-085.

[2]D. Helder, J. Thome, N. Mishra, G. Chander, X. Xiong, A. Angal, and T. Choi, "Absolute Calibration of Landsat Using a Pseudo Invariant Calibration Site", *IEEE Trans. Geosci. Remote Sens.*, vol. 51, no. 3, 2014.

[3] J. Storey, M. Choate, and K. Lee, "Landsat-8 Operational Land Imager On-Orbit Geometric Calibration and Performance" *Remote Sens.*, vol. 6, no.11127-11152, 2014.

[4] S. Biggar, J. Thome, and W. Wisniewski, “Vicarious radiometric calibration of EO-1 sensors by reference to high-reflectance ground tar-gets”, *IEEE Trans. Geosci. Remote Sens.*, vol. 41, no. 6, pp. 1174–1179, 2003. doi:10.1109/TGRS.2003.813211.

[5] G. Chander, “Catalog of worldwide test sites for sensor calibration”, *JACIE Workshop,* 2008, 26–28 March 2008, Fairfax, Va.

[6] C.R.N. Rao, and J. Chen, “Inter-satellite calibration linkages for the visible and near-infrared channels of the advanced very high resolution radiometer on the NOAA-7, -9, and -11 spacecraft”,*Int.J.Remote Sens*., vol. 16, pp. 1931–1942, 1995.Doi:10.1080/ 01431169508954530.

[7] H. Cosnefroy, M. Leroy, and X. Briottet, “Selection and characterization of Saharan and Arabian desert sites for the calibration of optical satellite sensors”, *Remote Sens. of Environ*., vol. 58, pp. 101–114, 1996. doi:10.1016/0034-4257(95)00211-1.

[8] C. Valorge, A. Meygret, L. Lebegue, P. Henry, A. Bouillon, R. Gachet, E. Breton, D. Leger, and F. Viallefont, “Forty years of experience with SPOT in-flight calibration. In Post-Launch calibration of Satellite Sensors”, Edited by S.A. Morain and A.M. Budge. *Int.Society for Photogrammetry and Remote Sens. ISPRS Book Series*, Vol. 2, pp. 119–133, 2004.

[9] D. Helder, B. Basnet, and D. Morstad, “Optimized identification of worldwide radiometric pseudo- invariant calibration sites”, *Can. J. Remote Sens.*, vol. 36, no. 5, pp. 527-539, 2010.

[10] D.G. Hadjimitsis, C.R.I. Clayton, A. Retalis, "The use of selected pseudo-invariant targets for the application of atmospheric correction in multi-temporal studies using satellite remotely sensed imagery", *Int. J. of Applied Earth Obs.and Geoinf.,* vol. 11, pp. 192–200, 2009.

[11] N. Mishra, D. Helder, A. Angal, T. Choi, X. Xiong, "Absolute calibration of optical satellite sensors using Libya 4 pseudo invariant calibration site", *Remote Sens*, vol. *6*, pp. 1327–1346, 2004.

[12] G. Chander, X. Xiong, A. Angal, T. Choi, "An assessment of African test sites in the context of a global network of quality-assured reference standards", *IEEE Trans. Geosci. Remote Sens.,* 2009.

[13] D. Morstad, D. Helder, "Use of pseudo invariant sites for long-term sensor calibration", *IEEE Trans. Geosci. Remote Sens.*, 2008

[14] W. Kim, T. He, D. Wang, C. Cao, and S. Liang, "Assessment of Long-term sensor radiometric degradation using time series analysis", *IEEE Trans. Geosci. Remote Sens.,* vol. 52, no. 5, 2014.

[15] A. Angal, X. Xiong, A. Wu, G. Chander, and T. Choi, "Multi-temporal cross-calibration of the Terra MODIS and Landsat 7 ETM+ reflective solar bands", *IEEE Trans. Geosci. Remote Sens.,* vol. 51, no. 4, 2013.

[16] Rajendra Bhatt, David R. Doelling, Daniel Morstad, Benjamin R. Scarino, and Arun Gopalan (2014). Desert-Based Absolute Calibration of Successive Geostationary Visible Sensors Using a Daily Exoatmospheric Radiance Model, *IEEE Trans. Geosci. Remote Sens.,* vol. 52, no. 6.

[17] N. Mishra, D. Helder, J. Barsi, B. Markham, "Continuous calibration improvement in solar reflective bands: Landsat-5 through Landsat-8", *Remote Sens. of Environ.,* vol. 185, pp. 7–15, 2016.

[18] Sudip Koirala, "Development of automatic cloud mask over PICS to support Landsat calibration", *Masters Graduate Thesis*: *South Dakota State University*, 2014.

[19] Stack Exchange available online https://physics.stackexchange.com/questions/15197/how-do-you-find-the-uncertainty-of-a-weighted-average?noredirect=1&lq=1 (last accessed: June 4th 2017).

[20] J. Roujean, "A Bidirectional Reflectance Model of the Earth's Surface for the Correction of Remote Sensing Data" *J. of Geo physical Research*, vol. 97, no. D18, pp. 20,455-20,468, 1992.

[21] "Natural Resources Canada", available online http://www.nrcan.gc.ca/node/14635 (last accessed: June 6th 2017).

[22] M. Shrestha, "Bi-Directional reflectance distribution function of the Algodones Dunes", *Masters Graduate Thesis: South Dakota State University*, 2016.

[23] Remote Sensing Technologies, "Test Site Catalog, Radiometry site resources catalog information", available online "https://calval.cr.usgs.gov/rst-resources/sites_catalog/radiometric-sites".

[24] USGS EROS, "Landsat-8 Users Handbook", EROS Sioux Falls, South Dakota, 2016, available online https://landsat.usgs.gov/documents/Landsat-8DataUsersHandbook.pdf (last accessed: June 6th 2017).

[25] R. Tabassum "Worldwide optimal PICS search", *Masters Graduate Thesis: South Dakota State University*, 2017.

APPENDIX A

A.1 Data Location for PNP Project:

All the results for this project are located in the SDSU Image Processing Lab 'iplabstorage (Z)' drive PNP folder.

1. Common for both L1T and BRDF Corrected Dataset:

Selected Image Dates: Z:\PNP\Basemap_image_dates\ PICSName_basemap_dates.txt

Geometrical Information for Selected L1T Images:
Z:\PNP\SubR\Ratiocal\PICSName\

ROI Location: Z:\PNP\ROI_Location\ PICSName_ROI_OPT.txt

Cloud-Free TOA Reflectance: Z:\PNP\cloudfree_TOA\
PICSName_cloudfree_TOA.mat

MATLAB Master Codes: Z:\PNP\MasterCodes\

2. L1T PNP data:

Trending Analysis: Z:\PNP\MasterPNP\ Normalized_AllPICS.xlsx

Z:\PNP\MasterPNP\ Master_SuperPICS.xlsx

PNP output data: Z:\PNP\MasterPNP\PICSName\

3. BRDF corrected PNP Data:

BRDF Coefficients: Z:\PNP\BRDF_Coeffs\ PICSName_L8_BRDFcoeffs.txt

Solar Zenith Angles for Selected Images:
Z:\PNP\sunzenith_angles\PICSName_sunzenith.txt

BRDF corrected TOA Reflectance:

Z:\PNP\MasterBRDFPNP\ PICSName_BRDF_corrected_TOA.mat

BRDF Corrected PNP output data: Z:\PNP\MasterBRDFPNP\PICSName\

Trending Analysis: Z:\PNP\MasterBRDFPNP\ Normalized_AllPICS.xlsx

Z:\PNP\MasterBRDFPNP\ Master_SuperPICS.xlsx

Drift Estimates and Worst-case bin Analysis:

Z:\PNP\MasterBRDFPNP\Drift for Individual PICS.xlsx

BRDF PNP output data: Z:\PNP\MasterBRDFPNP\PICSName\